https://doi.org/10.5194/egusphere-2025-67
Preprint. Discussion started: 31 March 2025

The Aerosol Limb Imager: Multi-spectral Polarimetric Observations of Stratospheric Aerosol

Daniel Letros[1], Liam Graham[1], Adam Bourassa[1], Doug Degenstein[1], Paul Loewen[1], Landon Rieger[1], and Nick Lloyd[1]

[1]Department of Physics & Engineering Physics, University of Saskatchewan, 116 Science Place, Saskatoon, Saskatchewan S7N 5E2, Canada

Correspondence: Daniel Letros (daniel.letros@usask.ca)

Abstract. The Aerosol Limb Imager (ALI) is designed to measure stratospheric aerosol by imaging limb-scattered sunlight. Each image taken by ALI is spectrally filtered at a tunable wavelength, and refined to consist of either horizontally or vertically polarized light. Novel to limb imaging, these polarized observations of ALI provide a means to isolate tangent altitudes which have signal contaminated by clouds. This avoids the ambiguity caused by clouds to be interpreted as aerosol in a retrieval. We present a polarized aerosol retrieval methodology which retrieves vertically resolved aerosol number density, and median radius of a unimodal log-normal distribution, in addition to a scalar width. We explore the cloud discrimination and aerosol retrieval of ALI in simulation as validation of the efficacy and the limits to the technique. We then apply the retrieval to three example sets of observations taken from the most recent high-altitude balloon flight of ALI. One set provides a nominal exemplar, while the other two represent more difficult retrieval conditions of an increasingly polarized atmosphere. We compare the aerosol extinction of ALI in all three exemplar cases to the best coincident extinctions of three space based instruments: the Stratospheric Aerosol and Gas Experiment (SAGE III), the Ozone Mapping and Profiler Suite (OMPS), and the Optical Spectrograph and InfraRed Imaging System (OSIRIS). We provide discussion to the agreement of all three cases against the comparison instruments with respected to the efficacy of our approach. However, we find the retrieved aerosol extinction of ALI in the nominal case is in good agreement to the extinction reported by SAGE III, OMPS, and OSIRIS while also yielding aerosol particle size information.

1 Introduction

The Aerosol Limb Imager (ALI) is a multi-spectral polarimetric imager with strong heritage at the University of Saskatchewan (Elash et al., 2016; Kozun et al., 2020). The design concept of ALI is to image sunlight scattered by the atmosphere in limb viewing geometry, and these images are then processed to profile atmospheric aerosol primarily in the stratosphere. Each image of the atmospheric limb taken by ALI is spectrally filtered by an acousto-optic tunable filter (AOTF), and taken at one of two linear polarizations used to discern clouds.

The ALI instrument concept is in development for long-term global aerosol observation on-board a satellite platform, and in the course of this development multiple variants of ALI have been built and tested. Although one such variant is meant

https://doi.org/10.5194/egusphere-2025-67
Preprint. Discussion started: 31 March 2025

for use on a high-altitude aircraft (Kozun et al., 2021), all other versions of ALI have been intended for use on high-altitude balloons. In this paper we discuss only the most recent variant of ALI designed for high-altitude ballooning, and the capability demonstrated during the last high-altitude balloon flight it took part in. The optical design of this ALI is discussed in (Letros et al., 2024) which pertains to polarimetric characterization. However, aspects of ALI design, performance, and data processing are provided here to contextualize the present work, and to establish the nature of the observations being used to demonstrate the aerosol profiling capability.

This capability is exhibited in two central ways. First is the retrieval of vertically resolved degree of polarization (DoP) profiles of the atmosphere using the polarized radiance profiles of ALI. The atmospheric DoP profiles identify tangent altitudes which are contaminated by light scattered from clouds, and can be removed from an aerosol retrieval. Second is the aerosol retrieval algorithm which optimizes an altitude dependant unimodal log-normal aerosol distribution. This algorithm retrieves altitudinal profiles of aerosol number density and median radius along with a scalar width (which is applied at all altitudes) to yield some particle size information in addition to the aerosol extinction. The methodology and limits of quantifying both the DoP and aerosol profiles is given alongside results in simulation supporting the efficacy.

We then apply this to three exemplar sets of observations taken from the last high-altitude balloon flight of ALI. The first set, called Scan 1, demonstrates ALI capability under nominal observation conditions. The other two sets, referred to as Scan 2 and Scan 3, show more difficult conditions. Scan 2 consists of sunrise observations, and Scan 3 is observing a highly polarized atmosphere. We conclude by comparing the aerosol retrievals of each ALI exemplar scan under our methodology to the nearest coincident aerosol extinction profiles reported by the Stratospheric Aerosol and Gas Experiment (SAGE III), the Ozone Mapping and Profiler Suite (OMPS), and the Optical Spectrograph and InfraRed Imaging System (OSIRIS).

2 The Aerosol Limb Imager

The optical design of ALI can be thought of as three sub-sections: a front end telescopic system which provides necessary angular magnification, the spectral and polarization selection (SPS) sub-system, and finally back end imaging optics. This system is shown in Fig. 1, and as mentioned more detail about the optical design of ALI can be found in (Letros et al., 2024). However, in the context of this work the SPS is the important section. The purposes of the SPS is to have ALI image either the horizontally polarized or the vertically polarized limb-scattered sunlight, and only at a selected wavelength. This is accomplished by a Liquid Crystal Rotator (LCR) which can be toggled to rotate the polarization of incoming light by (ideally) 90° or to let it pass unaltered, and an AOTF that is used to spectrally filter the light. The filtering is done by tuning the AOTF to diffract a selectable wavelength of light onto a different optical path, which is then imaged by the back end optics. The SPS also contains one linear polarizer after the LCR and another after the AOTF to further refine the polarized image (Letros et al., 2024; Kozun et al., 2021). The spectrally filtered and polarized images of ALI can then be converted into atmospheric radiance profiles used in aerosol retrievals.

In the operation of ALI, the LCR can be toggled to either an on or off state. This determines if the atmospheric scene being imaged is done so with the horizontally or vertically polarized light. However this polarimetric response is not ideal. The

https://doi.org/10.5194/egusphere-2025-67
Preprint. Discussion started: 31 March 2025

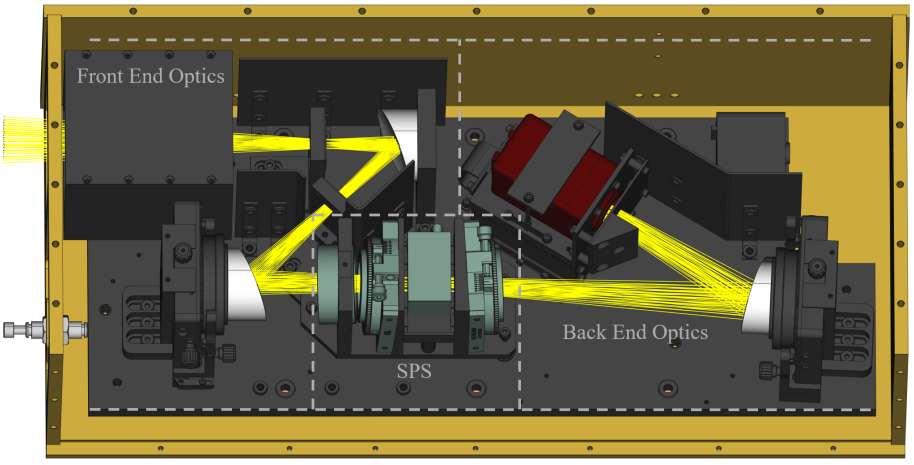

Figure 1. Render of ALI optical layout. The front end optics consists of a baffle, stops, and two off-axis parabolic mirrors providing angular magnification. The SPS is comprised of four components (listed front to back): the LCR, a vertically orientated linear polarizer, the AOTF, and a horizontally orientated linear polarizer. The back end optics comprises of one off-axis parabolic mirror focusing a spectrally filtered and polarized image onto the detector.

polarimetric impurity varies over wavelength along with the spectral response of the AOTF which also varies over wavelength. As the AOTF is tuned to diffract different wavelengths, the transmission (diffraction efficiency) and width of the AOTF spectral bandpass also changes. This, in addition to other non-idealities such as detector characteristics, will of course affect the interpretation of raw ALI images (pixels of a digital number DN) with respect to the desired quantity of atmospheric radiance (units of $\mathrm{photons/s/cm^2/sr/nm}$). To establish the connection between the information used in our aerosol retrievals, and the raw observations of ALI we provide a discussion of instrument performance and characterization below.

2.1 AOTF Diffraction Efficiency and Spectral Bandpass

The spectral performance of ALI is principally determined by the performance of the AOTF, which can be thought of as an adjustable optical filter. In order to quantify the spectral information ALI observes, the bandpass and diffraction efficiency of the AOTF needs to be known for the operating range. The technique to do this follows from (Kozun et al., 2020), and uses a spectrometer to measure the un-diffracted light of the AOTF with and without diffraction being active for a range of tuned frequencies (center filter wavelengths). The diffraction efficiency at a tuned wavelength of the AOTF is taken as the peak percentage difference between the diffracted and non-diffracted signals. The spectral bandpass of ALI for a tuned frequency is taken as the full-width half-max (FWHM) of the diffraction response. Figure 2 shows this process and results over the operating range of the AOTF.

We must note that to avoid very significant computational requirements of modelling a high-resolution spectrum for the aerosol retrieval, we treat all measured photons at a tuned wavelength to be of that tuned wavelength. Effectively this ignores the change of wavelength within the resolution of a spectral response. To account for the net photons ALI measures at each

https://doi.org/10.5194/egusphere-2025-67
Preprint. Discussion started: 31 March 2025

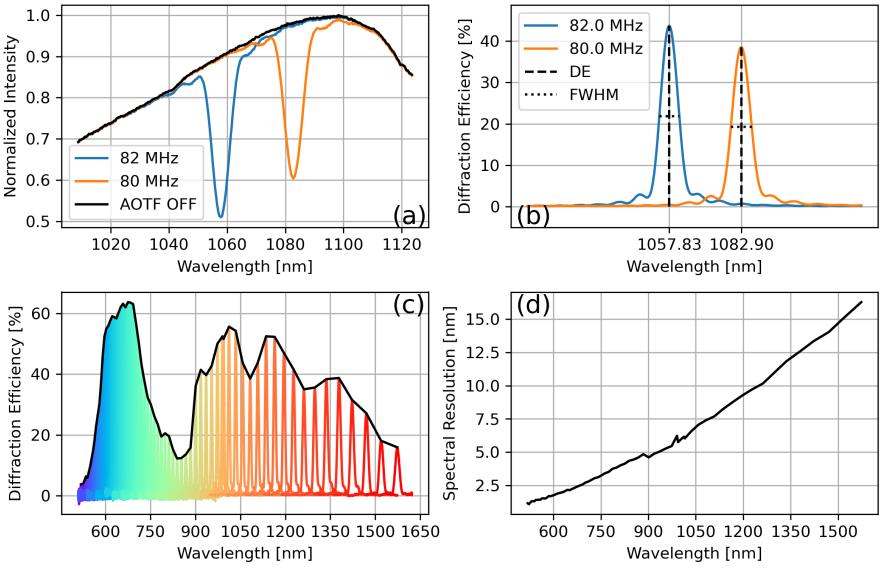

Figure 2. AOTF spectral performance. (a) Measurement process of AOTF spectral response at two tuned frequencies. These frequencies correspond to shifting diffraction to a desired wavelength. This diffracted light is imaged by ALI. 82 MHz (1058 nm) shown in blue and 80 MHz (1083 nm) shown in orange. The total un-diffracted light with no active diffraction shown in black. (b) Measurements of plot (a) shown as two spectral responses. The diffraction efficiency (AOTF transmission) is calculated by peak response, and spectral resolution is defined as the FWHM of the response. (c) Diffraction efficiencies of the AOTF sampled across the full operating range of the AOTF as a function of diffracted wavelength. (d) The spectral resolution for the full range of the AOTF as a function of diffracted wavelength.

tuned wavelength, the area of each spectral response is calculated by integrating the measured diffraction responses with respect to wavelength after they have been normalized by the diffraction efficiency. This area yields a scalar factor for each tuned wavelength that is used to account for the nm dependence of radiance as the images are processed.

2.2 Polarimetric Response

As mentioned before, ALI is designed to image the vertically polarized limb-scattered sunlight of the atmosphere, or the horizontally polarized light of the atmosphere depending on the configuration of the LCR. However to be more precise, we consider all polarimetric behaviour in terms of the Stokes parameters I, Q, U, and V (following their typical definitions (Bass and et al, 2010)) and the Mueller matrices which transform them. Each pixel of an ALI image measures I', which is produced by transforming the atmospheric Stokes vector of that pixel's line of sight by the Mueller matrix of ALI:

$$I' = \begin{bmatrix} 1 & 0 & 0 & 0 \end{bmatrix} \mathbf{M_{ALI}} \begin{bmatrix} I_{\text{atmo}} & Q_{\text{atmo}} & U_{\text{atmo}} & V_{\text{atmo}} \end{bmatrix}^T \tag{1}$$

https://doi.org/10.5194/egusphere-2025-67
Preprint. Discussion started: 31 March 2025

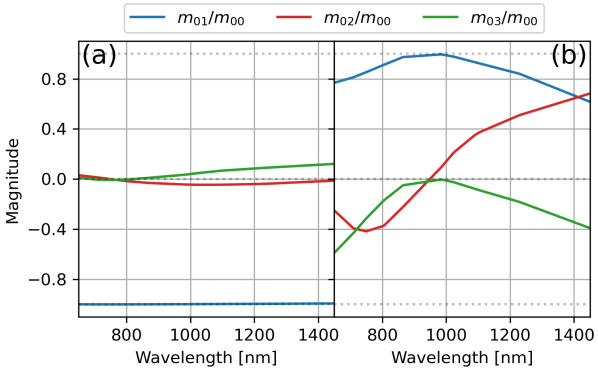

Figure 3. Non-ideal polarimetric response of ALI (Letros et al., 2024) shown as normalized coefficients of the first row of the Muller matrix, which dictates the measured Stokes parameter I'. Plot (a) is the response of the LCR on state. Plot (b) is the response of the LCR off state. The coefficient of m_{01}/m_{00} shows the proportional transference of Q_{atmo} into I'. Likewise, m_{02}/m_{00} and m_{03}/m_{00} show the same for U_{atmo} and V_{atmo} respectively. An ideal ALI response would have $m_{01}/m_{00} = -1$ in the LCR on state, $m_{01}/m_{00} = 1$ in the LCR off state, as well as $m_{02}/m_{00} = 0$ and $m_{03}/m_{00} = 0$ for both cases - i.e. purely vertical linear polarization with the LCR on, and purely horizontal linear polarization with the LCR off.

where $\mathbf{M_{ALI}}$ is an appropriate Mueller matrix of ALI for the measurement. Since ALI has two LCR states defining the polarimetric behaviour, ALI effectively has two wavelength dependant Mueller matrices - one matrix for when the LCR is toggled on, and another for when it is toggled off. The work of (Letros et al., 2024) describes the polarization characterization we apply to ALI, and this procedure produces the full 16 element Mueller matrix at the required states of interest. Therefore we do not discuss this topic with depth here.

However to provide context to discussion in the present work, when the LCR is enabled (referred to as the "LCR on" state) ALI behaves as an imperfect vertical linear polarizer. Likewise, when the LCR is not enabled (referred to as the "LCR off" state) ALI acts as an imperfect horizontal linear polarizer. This non-ideal response of ALI (in the Stokes basis defined by ALI) as found in (Letros et al., 2024) is shown in Fig. 3.

2.3 Image Correction

Each pixel in an ALI image measures a signal reported as the raw detector units of DN, and we convert this measurement to the more meaningful measure of radiance in units of $\mathrm{photons/s/cm^2/sr/nm}$. In this conversion, we also handle correction of instrumentation effects such as dark current, photo response non-uniformity, optical flat fielding, and bad pixels. The resulting tool of this process is a database of pixel-by-pixel coefficients which can synthetically reproduce the ALI measurement of a calibrated broadband integrating sphere of known (randomly polarized) spectrum. These synthetic images can be made for all wavelengths, LCR states, and exposure times of interest. Furthermore, since they reproduce the spatially flat and full-

https://doi.org/10.5194/egusphere-2025-67
Preprint. Discussion started: 31 March 2025

field conditions of the integrating sphere, they can be used to relate the ALI measurements to the external source each pixel measured. We provide a summary overview to the construction and application of this database within scope of this paper.

The database of coefficients begins by characterizing the dark behaviour of the ALI detector. As typical, we collect a large set of images at various exposure times when no light is present within the optics. While the focal plane array of the detector is thermally controlled by a thermoelectric cooler, the temperature of the other electronics in the detector have an impact on the observed dark signal. We analyse the dark image set for this dependence and fit an exponential form to each pixel quantifying this behaviour. All pixels are then corrected to a common electronic temperature according to these fitted curves. The temperature corrected images are then used to determine the expected dark signal each pixel is expected to produce for a given exposure time. This is quantified by another regression with respect to exposure time, and is mostly linear. However, some non-linear behaviour is observed for short exposure times which we capture with another exponential regression. Note that any detector pixels which fail to regress well and/or are statistical outliers are marked as bad pixels in the dark calibration. These pixels are not carried forward in image processing.

Following this, a large collection of images is taken of the calibrated integrating sphere mentioned before at a fixed intensity. This set of images consists of various exposure times at each tuned wavelength of the AOTF, and both toggled states (polarizations) of the LCR . All images are corrected for the dark behaviour as discussed above, and a linear regression is applied which quantifies each pixels response with respect to exposure time in each configuration (AOTF tuned frequency and LCR state) of ALI. This fitting can then be used to constructed an expected ALI image given a flat uniform source after dark correction. Similar to the bad pixel identification of the dark regression, any pixel which fails under illumination is also marked as bad and not carried forward in image processing.

Figure 4 shows an example of synthetic image construction compared against an actual ALI image. As this example shows, the synthetic image provides a faithful recreation of the actual ALI measurement. The error of this reproduction, as demonstrated by the histogram, is on the order of the square root of the DN values in the images. This indicates the error is of the expected shot noise.

Since the source of this exercise is known and spatially flat, these synthetic images effectively provide the corrections of photo response non-uniformity and optical flat fielding. In addition, the source spectrum of the calibrated integration sphere is known. Therefore, we can also provide an absolute calibration by relating the detector counts to the source radiance. This is done by taking the spectrum of radiance used in the calibration and integrating it over the AOTF bandpass to determine a unit conversion to from DN into $\mathrm{photons/s/cm^2/sr}$ (radiance without the wavelength dependence). The wavelength dependence is introduced back into this conversion in accordance with the discussion in Section 2.1 to ultimately give radiance in $\mathrm{photons/s/cm^2/sr/nm}$. The uncertainty on each pixel is then calculated as a function of shot noise of the corrected image, dark shot noise at the same exposure time, and detector read out noise.

A final concern we address in image correction is the issue of (potential) stray light. A unique advantage of AOTF technology is that if an image is taken where there is no diffraction, then that image is a measure of the stray light in the optical system - and one that is applicable to the illumination conditions outside of the instrument when the desired measurements (AOTF diffraction on) is being taken. The image acquisition strategy of ALI is to take an image without diffraction (AOTF off) for

https://doi.org/10.5194/egusphere-2025-67
Preprint. Discussion started: 31 March 2025

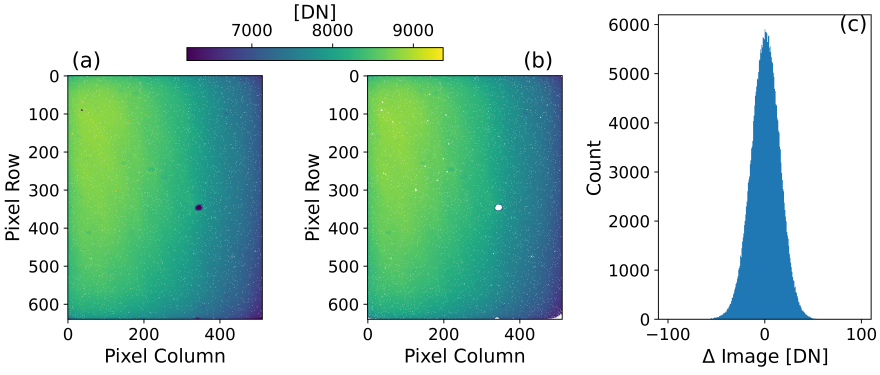

Figure 4. Example comparison of synthetic image construction for ALI correction. (a) A single ALI image of the calibrated integrating sphere. AOTF is tuned to diffract 1450 nm, the LCR is off, and an exposure time of 0.450 seconds is used in this example. Dark correction has been applied. White dots in this image indicate the bad pixels as determined by the dark correction. (b) A synthetic reproduction of the real image shown in the left plot constructed from the database of calibration coefficients. White (bad) pixels seen in this image are determined as pixels with non-ideal responses and discarded. (c) A histogram of all (non-bad) pixel values after the synthetic (middle) image is subtracted from the real (left) image.

every image with diffraction (AOTF on). The AOTF off images are corrected in the same manner as the AOTF on images to produce an image of stray light. This stray light image can then be subtracted off the AOTF on image. Note that this method effectively deals with internally scattered stray light but does not handle the impact of out-of-field stray light for a given scientific image. This is mitigated with careful baffling of the input aperture.

3 Flight Campaign and Spectral Results

The ALI measurements we use in the aerosol retrievals of the present work are taken from the most recent high-altitude balloon flight of ALI. This flight began on August 21st, 2022, 11:30 pm (local) out of the Timmins stratospheric balloon base (attached to the Victor M. Power airport) in Ontario, Canada. ALI was situated on the balloon gondola and orientated such that when the gondola is flat and level, the highest lines of sight (top pixels of the ALI detector) would be horizontal and with tangent locations on the instrument itself. ALI ascended to a float altitude of ≥ 35 km roughly two hours after the 11:30 pm launch. However, being a night launch ALI only began useful observations as the sun was rising. At this point in the flight the gondola was steered to maintain a solar azimuth angle (SAA) of 60°.

During the flight, ALI took images in sets which make up an ALI science scan. A full science scan consisted of imaging 710 nm, 750 nm, 805 nm, 865 nm, 985 nm, 1025 nm, 1090 nm, 1105 nm, 1230 nm, and 1450 nm. At each wavelength an image with the LCR off (horizontal polarization) is taken, then AOTF off, then LCR on (vertical polarization), and AOTF off again. The LCR on and LCR off images have the AOTF on to image the atmospheric limb, while the AOTF off imaging providing stray light correction. However, for the scope of the present work we select only three of these science scans for demonstration.

https://doi.org/10.5194/egusphere-2025-67
Preprint. Discussion started: 31 March 2025

Table 1. Science Scan Summary

Scan	UTC [2022-08-22]	Altitude [m]	Lat/Lon/Heading [deg]	SAA [deg]	SZA [deg]	SSA [deg]
1 (nominal)	14:06:13	36314	48.6/-82.8/172.4	60.0	56.0	65.2
2	10:30:26	37070	48.9/-82.5/10.3	60.1	90.8	60.2
3	15:19:13	36764	49.0/-83.1/191.1	59.9	46.2	68.4

As the gondola was aloft during the near 13 hours of flight, sequences of images were taken and categorized into different scans. Three of these scans are selected for study in this work and their metrics are summarized here. Altitude, latitude, and longitude all refer to the position of the flight gondola. Heading, solar azimuth angle (SAA), solar zenith angle (SZA), and solar scattering angle (SSA) are all given with respect to ALI. All properties are reported as the average of the complete scan.

Furthermore, for each of the three scans we retrieve aerosol using only 750, 1025, and 1230 nm. This is to avoid spectral contamination from trace gas absorption in the wings of the AOTF passband at the other channels.

The first scan we select is of reasonably nominal conditions for ALI to observe. The balloon gondola was relatively stable for this scan compared to most others taken during the flight, and ALI observes an obvious cloud layer in the lower portion of these images with clear sky perceived above. The other two scans we select present more difficult observation conditions both in terms of (relative) gondola stability and observational conditions. The second scan we select is taken as the sun rises, and another cloud layer is seen (at least partially) illuminated in the lower portion of the image. Finally the third scan we select consists of no visible clouds, but a highly polarized atmosphere is measured (see results in Fig. 14). We show the observations of each scan in Fig. 5, and for additional context Table 1 summarizes the mean attributes of each selected scan. Note that a significant difference of Scan 2 is that it is looking north, while the other two scans are looking south. The difference in latitudinal look direction implies that Scan 2 is observing a different atmospheric state than Scan 1 and Scan 3.

An additional reason these three scans are selected as exemplars is because of the dominance between horizontally and vertically polarized radiance they show. Observing the radiance profiles of Fig. 5, it is clear to see that Scan 1 shows a reasonably even balance between the vertically and horizontally polarized light, while Scan 2 is vertically dominated, and Scan 3 is horizontally dominated. This relative balance and transition between vertically and horizontally dominated light is to be expected from the solar geometry of each scan, but this provides contrasting test cases for ALI.

4 Retrieval Methodology and Prototyping

Here we discuses the concepts behind the inversion methodology used by the present work, as well as also providing results of prototyping the algorithms in simulation with known true states. This not only demonstrates the efficacy of the retrieval algorithms we present here, but also contextualizes the results we obtain when applying the algorithms to the real data of the flight in Section 5. As mentioned before, the aerosol profiling ability of ALI has two main aspects we discuss here. The first aspect is determining altitudes of cloud contamination using retrieved DoP profiles of the atmosphere. These altitudes are then passed on to the second aspect of the (separate) aerosol retrieval and marks the lower altitude limit to retrieve. Facilitating both

https://doi.org/10.5194/egusphere-2025-67
Preprint. Discussion started: 31 March 2025

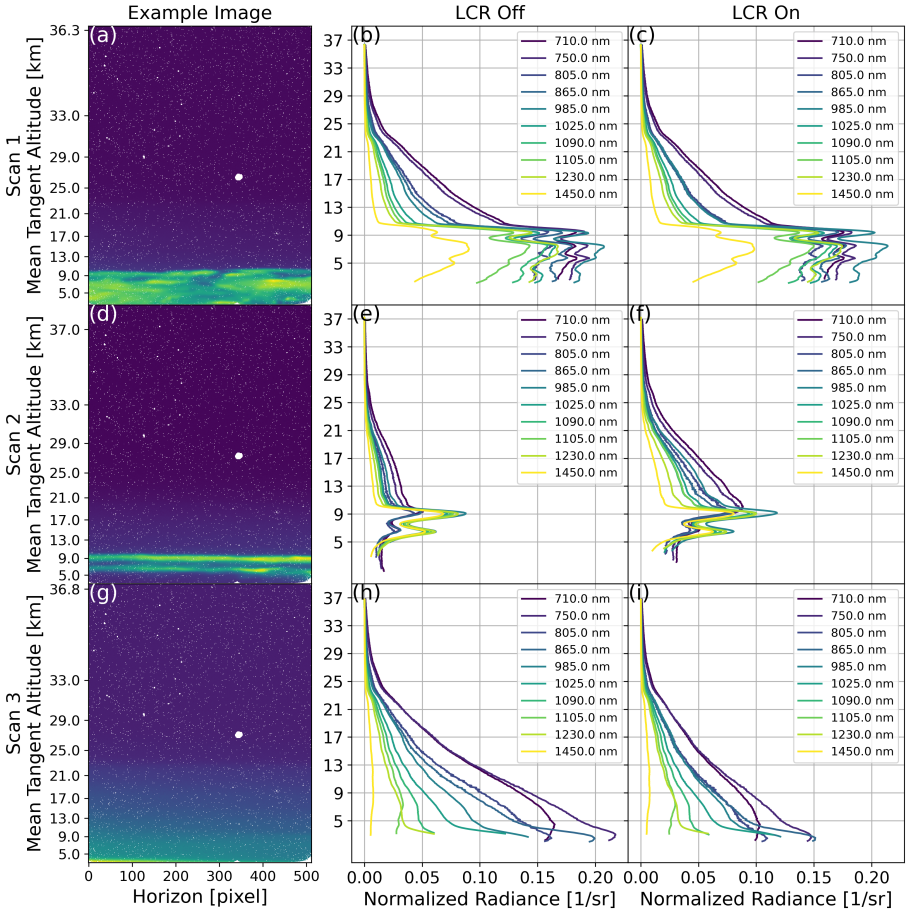

Figure 5. Observations of all three ALI scans used in the present work. (a, b, c) Scan 1 observations. (d, e, f) Scan 2 observations. (g, h, i) Scan 3 observations. (a, d, g) Example images from the three different scans taken at 1230 nm with the LCR off. (b, e, h) Radiance profiles of different wavelengths with the LCR off (horizontally dominate polarization). (c, f, i) Radiance profiles of different wavelengths with the LCR on (vertically dominate polarization). The radiance profiles of (b, c, e, f, h, i) are constructed by following Section 2.3 to convert images into $\mathrm{photons/s/cm^2/sr}$ from DN. Then following Section 2.1 to obtain units of $\mathrm{photons/s/cm^2/sr/nm}$. The images are column binned and normalized by the solar irradiance produced by a radiative transfer forward model (see Section 4.3) yielding profiles of $1/\mathrm{sr}$.

the DoP and aerosol retrievals is the need to estimate an effective albedo factor to use in the forward modelling, this will also be briefly discussed.

Both aerosol and DoP retrievals have separate implementations of the same underlying inversion theory, which is based in the standard approach of (Rodgers, 2000). This approach attempts to find the statistically most likely state vector $\boldsymbol{x}$ given
180 the observations encapsulated in measurement vector $\boldsymbol{y}$, under the assumption of normally distributed probability density functions. For non-linear systems, this is iteratively done using Equation 5.35 of (Rodgers, 2000):

https://doi.org/10.5194/egusphere-2025-67
Preprint. Discussion started: 31 March 2025

$$\boldsymbol{x}_{i+1} = \boldsymbol{x}_i + (\mathbf{S}_a^{-1} + \mathbf{K}_i^T \mathbf{S}_\epsilon^{-1} \mathbf{K}_i + \gamma \mathbf{D}_n)^{-1} \{\mathbf{K}_i^T \mathbf{S}_\epsilon^{-1} [\boldsymbol{y} - \mathbf{F}(\boldsymbol{x}_i)] - \mathbf{S}_a^{-1} [\boldsymbol{x}_i - \boldsymbol{x}_a]\} \tag{2}$$

where i notes the iteration, the a-priori state vector $\boldsymbol{x}_a$ encapsulates the a-priori knowledge of the state, $\mathbf{K}$ is a Jacobian, $\mathbf{S}_a$ is the covariance of $\boldsymbol{x}_a$, and $\mathbf{S}_\epsilon$ is the covariance of $\boldsymbol{y}$. $\mathbf{D}$ is a customizable dampening matrix which restricts elements of the optimization from changing too much. The scalar γ controls the dampening strength of $\mathbf{D}$ and is adjusted to be larger or smaller based on the change of the underlying cost function that is being minimized. Ideally, $\gamma \to 0$ as the retrieval progresses. An additional matrix, the averaging kernel, is defined as $\mathbf{A} = (\mathbf{S}_a^{-1} + \mathbf{K}_i^T \mathbf{S}_\epsilon^{-1} \mathbf{K}_i)^{-1} \mathbf{K}_i^T \mathbf{S}_\epsilon^{-1} \mathbf{K}$ and yields useful metrics about the retrieval - such as information content, and vertical resolution.

The remaining element of Equation 2 for definition is $\mathbf{F}(\boldsymbol{x}_i)$. This is the forward model of the inversion which models the same kind of observations within $\boldsymbol{y}$ that would be produced by the given state $\boldsymbol{x}_i$. The forward modelling of the present work is done with the radiative transfer model SASKTRAN (Bourassa et al., 2008; Zawada et al., 2015) coupled with an ALI simulator following the heritage of (Kozun et al., 2020). Briefly speaking, SASKTRAN calculates the expected atmospheric Stokes vectors, as well the polarized Jacobian $\mathbf{K}$, given some atmospheric state and observational geometry. The instrument simulator adjusts the Stokes basis to account for the attitude of the gondola, and then applies the appropriate ALI Mueller matrix to model the LCR on or off observation. The only significant exception to this forward modelling dynamic is in the DoP retrievals where SASKTRAN is only used to produce a-priori information, but this is discussed in Section 4.2.

During our retrievals, Equation 2 is run until convergence is determined. This is evaluated based on an established method of evaluating the cost function χ^2 (Rodgers, 2000; Zawada et al., 2018):

$$\chi^2 = [\mathbf{F}(\boldsymbol{x}) - \boldsymbol{y}]^T {\mathbf{S}_\epsilon}^{-1} [\mathbf{F}(\boldsymbol{x}) - \boldsymbol{y}] + [\boldsymbol{x_a} - \boldsymbol{x}]^T \mathbf{S}_a^{-1} [\boldsymbol{x_a} - \boldsymbol{x}] \tag{3}$$

for both a non-linear and linear iteration. The ratio of these two χ^2 values is taken, and if this ratio is one within a specified tolerance - taken as 0.001 in the present work - then it is an indication the linear estimate is now as good as the non-linear estimate and a solution has been reached. At this point, the uncertainty of the final state estimation $\hat{\boldsymbol{x}}$ can be determined by the solution covariance matrix $\hat{\mathbf{S}}$ (Equation 5.13 (Rodgers, 2000))

$$\hat{\mathbf{S}} = (\hat{\mathbf{K}}^T \mathbf{S}_\epsilon^{-1} \hat{\mathbf{K}} + \mathbf{S}_a^{-1})^{-1} \tag{4}$$

There are two potentially notable deviations we make from the common approaches of this inversion technique. The first is that typically for atmospheric inversions one will implement a regularization matrix in place of $\mathbf{S}_a^{-1}$. We do not adopt this approach as we found it harmed vertical resolution of our retrievals more than improving the smoothness of the state vectors. We simply specify a-priori uncertainties as discussed later. Second, our retrievals use measurement and state vectors of large dynamic range which tends to produce ill-conditioned inversions. Since the inversion technique of (Rodgers, 2000) is a variant of the Extended Kalman Filter (Kalman, 1960; McGee et al., 1985; Becker, 2023; Grewal, 1993), we adopt the Singular Value

https://doi.org/10.5194/egusphere-2025-67
Preprint. Discussion started: 31 March 2025

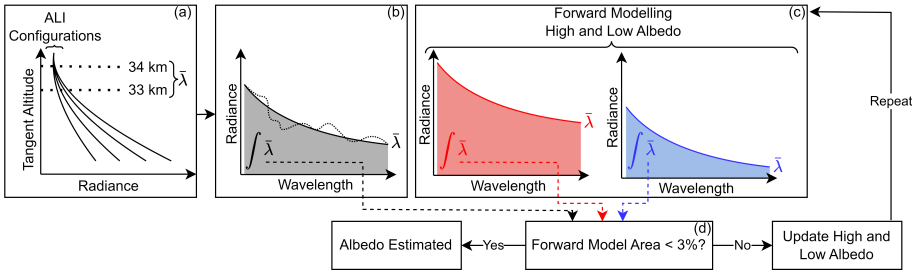

Figure 6. Flow diagram of the albedo estimation algorithm. (a) Radiance profiles of different configurations (LCR state and wavelength) of ALI are collected, and for each a mean radiance value between 33 km and 34 km is found. (b) The values collected in step (a) have measurement noise. For this reason these values plotted as a function of wavelength will vary (represented with the dotted line) about the expected background trend (solid line). The step (a) values are used in a non-linear regression to represent the trend in the data. This curve is then integrated producing a spectral area as the metric for the albedo estimation. (c) The configurations of step (a) are now forward modelled (without noise) for both a high (beginning at 1.0) and low (beginning at 0.0) albedo value. For each modelled albedo, the spectral area is found in the same manner as step (b). (d) The areas are compared and the albedo value with the lower percent error is taken as the current albedo estimation. If agreement is not within 3% new high and low albedo values are calculated by perturbing the estimated albedo proportionally to twice that of the percent difference. The cycle of steps (c) and (d) are repeated until agreement is found.

Decomposition - Kalman Filter (Wang et al., 1992; Kulikova and Tsyganova, 2017) to combat this. In brief, this method uses singular value decomposition to enforce positive definite matrices and largely propagates the inversion in eigenvector space.

4.1 Albedo Estimation

The albedo estimation aims to find the albedo to use in the radiative transfer forward model which best matches the observed radiance at high-altitudes over the available spectrum of ALI in each scan. This is a typical step for limb scatter aerosol retrievals (Bourassa et al., 2012). Once this is determined we consider it fixed for the forward modelling purposes of both the DoP retrieval and the aerosol retrieval. While the albedo could be included as a parameter of the aerosol retrieval proper, we take this ad-hoc approach to constrain and simplify the aerosol retrieval forward modelling rather than to include it as a member of the state vector $\boldsymbol{x}$ to be optimized. In addition, high-altitude normalization of the aerosol retrieval's measurement vectors is a strategy to mitigate systematics and forward modelling error such as improper albedo (Rieger et al., 2018).

For purposes of the albedo estimation, we define high-altitude as all observed tangent altitudes between 33 km and 34 km in the science scan. It is expected that at these altitudes the influence of aerosol is minimal. Therefore, adjusting albedo in a forward modelled Rayleigh (no aerosol) scattering atmosphere to match the observed high-altitude signal will provide an *effective* albedo accounting for the up-welling radiation. The measure we take to quantify the albedo is the integration of the high-altitude radiance with respect to wavelength. A flow diagram outlining this algorithm is provided in Fig. 6.

As an example evaluation, this technique was used against a forward modelled atmosphere of known true state albedo of 0.6, and inclusion of a GloSSAC (Thomason et al., 2018) aerosol extinction profile. In this exercise, the final albedo estimation of

https://doi.org/10.5194/egusphere-2025-67
Preprint. Discussion started: 31 March 2025

Table 2. Estimated albedo values of ALI example scans.

Scan #	1	2	3
Estimated effective albedo	0.833	0.3	0.615

Scan 2 is insensitive to albedo. Value of 0.3 is assigned, not estimated.

0.654 was found, which we consider to be a reasonable estimation of the 0.6 true state. Following this, we show the estimated albedo of each example ALI scan in Table 2. Note that Scan 2 proved insensitive to changes in albedo, which is expected from sunrise conditions, so we simply assign a value of 0.3 here. However, the low sun condition also means the retrieval is quite insensitive to the large uncertainty in albedo for this case.

4.2 Cloud Discrimination

A primary motivation for the polarimetry of ALI is to discriminate scattering by clouds and scattering by aerosol. This is so the contribution of cloud scattering is not attributed to atmospheric aerosol in the retrieval. Typical approaches to this problem study the vertical gradient of limb radiance profiles and how it differs over wavelength (Chen et al., 2016), but this is still prone to identifying aerosols with larger particle sizes as clouds. However, scattering by clouds will tend to reduce the DoP (Hansen, 1971; Deirmendjian, 1964), so relative changes in polarized light can be used as a metric to determine if limb-scattered signal was influenced by cloud or not.

The goal of the analysis here is to acquire a vertical profile of the DoP. While this is useful in itself to identify altitudinal regions of different scattering behaviour, for the purposes of the present work we focus only on determining the lower limit of the aerosol retrieval. That is to say, quantitatively identify a tangent altitude in which cloud scattered light becomes significant as indicated by a reduction in the atmospheric DoP. Aerosol retrieved using measurements above this tangent altitude will be free of any notable ambiguity with cloud.

The atmospheric DoP can be directly approximated from ALI measurements, which Section 4.2.1 discusses. Unfortunately, the non-ideal behaviour of the ALI polarimetric response reduces the effectiveness of this approximation. Therefore, we also present an approach to retrieve the Stokes parameters of the atmosphere in the Stokes basis of ALI in Section 4.2.2. This DoP retrieval provides a more robust analysis of the atmospheric DoP and is the method we employ for cloud identification in Section 5.

4.2.1 Direct Approximation of DoP

As discussed in Section 2, ALI measures two different polarization states for each wavelength λ depending on if the LCR is engaged or not. Ideally, the measurement with the LCR off (I'_{LCRoff}) would have ALI measure horizontally polarized light ($|E_x|^2$), while the LCR on measurement (I'_{LCRon}) would measure vertically polarized light ($|E_y|^2$). However as Section 2.2 addresses, the Mueller matrix of ALI does not yield this ideal response and the performance is wavelength dependant. Despite

https://doi.org/10.5194/egusphere-2025-67
Preprint. Discussion started: 31 March 2025

this, vertical profiles of the Stokes parameters I and Q, as well as the DoP (P) can be *approximated* (noted with $\tilde{I}$, $\tilde{Q}$, and $\tilde{P}$ respectively) using the I'_{LCRon} and I'_{LCRoff} observations like those shown in Fig. 5. Equations 5 to 7 show these relations.

$$I(\lambda) = |E_x(\lambda)|^2 + |E_y(\lambda)|^2 \qquad \approx \tilde{I}(\lambda) = I'_{\text{LCRoff}}(\lambda) + I'_{\text{LCRon}}(\lambda) \tag{5}$$

$$Q(\lambda) = |E_x(\lambda)|^2 - |E_y(\lambda)|^2 \qquad \approx \tilde{Q}(\lambda) = I'_{\text{LCRoff}}(\lambda) - I'_{\text{LCRon}}(\lambda) \tag{6}$$

$$P(\lambda) = \frac{\sqrt{Q(\lambda)^2 + U(\lambda)^2 + V(\lambda)^2}}{I(\lambda)} \approx \tilde{P}(\lambda) = \frac{|\tilde{Q}(\lambda)|}{\tilde{I}(\lambda)} \tag{7}$$

4.2.2 Retrieval of DoP

To compensate for the polarimetric response of ALI which Equations 5 to 7 fail to do, we present an approach to retrieve the Stokes parameters of the atmosphere in the Stokes basis of ALI. Here we conceptualize the inverse problem as largely separated from the physics of radiative transfer (unlike Section 4.3) and consider each wavelength independently of the others. That is to say the measurement vector is the LCR on and off measurements at only one wavelength, and the retrieval is repeated separately for each wavelength.

An individual λ selected for analysis will have its measurement vector $\boldsymbol{y}(\lambda)$ constructed as

$$\boldsymbol{y}(\lambda) = \begin{bmatrix} I'_{\text{LCRon}}(\lambda)_{(0)} & \dots & I'_{\text{LCRon}}(\lambda)_{(n)} & I'_{\text{LCRoff}}(\lambda)_{(0)} & \dots & I'_{\text{LCRoff}}(\lambda)_{(n)} \end{bmatrix}^T \tag{8}$$

where the numbered indices n indicate detector pixels which directly correspond to tangent altitudes at the time the observation was taken. We then define the state vector as attitudinal profiles of Poincaré parameters (Bass and et al, 2010) as

$$\boldsymbol{x}(\lambda) = \begin{bmatrix} I(\lambda)_{(0)} & \dots & I(\lambda)_{(n)} & P(\lambda)_{(0)} & \dots, P(\lambda)_{(n)} & \theta(\lambda)_{(0)} & \dots & \theta(\lambda)_{(n)} \end{bmatrix}^T \tag{9}$$

where $I(\lambda)$ is the Stokes parameter I of the atmosphere at λ, $P(\lambda)$ is the degree of polarization at λ, and $\theta(\lambda)$ is the orientation of the polarization ellipse major axis at λ. With an assumption of no circularly polarized light, the Poincaré latitude is taken as zero. Describing the Stokes parameters with respect to the Poincaré sphere provides a convenient framework for enforcing the constraints of the system (such as DoP ≤ 1) in the forward modelling. With this, the forward model of each pixel (tangent altitude) n of the retrieval can then be described as

$$I'_{\text{LCRon}}(\lambda)_{(n)} = \begin{bmatrix} 1 & 0 & 0 & 0 \end{bmatrix} \mathbf{M_{on}}(\lambda) \begin{bmatrix} I(\lambda)_{(n)} & I(\lambda)_{(n)} P(\lambda)_{(n)} \cos(2\theta(\lambda)_{(n)}) & I(\lambda)_{(n)} P(\lambda)_{(n)} \sin(2\theta(\lambda)_{(n)}) & 0 \end{bmatrix}^T \tag{10}$$

$$I'_{\text{LCRoff}}(\lambda)_{(n)} = \begin{bmatrix} 1 & 0 & 0 & 0 \end{bmatrix} \mathbf{M_{off}}(\lambda) \begin{bmatrix} I(\lambda)_{(n)} & I(\lambda)_{(n)} P(\lambda)_{(n)} \cos(2\theta(\lambda)_{(n)}) & I(\lambda)_{(n)} P(\lambda)_{(n)} \sin(2\theta(\lambda)_{(n)}) & 0 \end{bmatrix}^T \tag{11}$$

https://doi.org/10.5194/egusphere-2025-67
Preprint. Discussion started: 31 March 2025

where $\mathbf{M_{on}}(\lambda)$ and $\mathbf{M_{off}}(\lambda)$ are the full descriptions of the ALI Mueller matrix in the LCR on and off states for λ. These are obtained from the work of (Letros et al., 2024) which is directly applicable here. $\mathbf{S}_\epsilon$ of this inversion is constructed identically to that described in Section 4.3, that is to say a diagonal matrix of the measurement noise. $\mathbf{S_a}$ is also a diagonal matrix with standard divinations of $\sigma_I = 0.005$, $\sigma_P = 0.05°$, and $\sigma_\theta = 0.1°$ which were selected via prototyping the algorithm. Finally, $\mathbf{D}$ is constructed from the diagonal of $\mathbf{K}^T\mathbf{S}_\epsilon\mathbf{K}$, where naturally $\mathbf{K}$ is constructed from the derivatives of Equations 10 and 11. $\mathbf{D}$ is then additionally altered to decrease the dampening of $I(\lambda)_{(n)}$ for n corresponding to tangent altitudes below 15 km, as well as increase the dampening of $\theta(\lambda)_{(n)}$. The purpose of this is so the beginning iterations of the retrieval will favour attributing large changes of $\boldsymbol{y}(\lambda)$ expected from clouds to a change of the total light instead of the polarization parameters (i.e. favour depolarized the radiance). On further iterations γ will tend to zero disabling this dampening affect.

A radiative transfer model is not directly used in this retrieval, but SASKTRAN is used as a tool for constructing a-priori state profiles at different solar geometry, as well as prototyping Stoke behaviour of atmospheric radiance with respect to different atmospheric conditions. This prototyping indicated that at fixed solar geometry, the θ state is reasonably insensitive to atmospheric properties except for the effective albedo. For this reason the albedo retrieval of Section 4.1 is used to construct an appropriate a-priori θ profile. This assumption of a reasonably accurate θ profile is also why θ is additionally damped in $\mathbf{D}$ instead of the DoP.

As demonstration of efficacy, we present results of the method in retrieving a known true state in simulation at 1105 nm. This simulation uses the attitude and solar geometry of the Scan 1. The true state Poincaré (Stokes) profiles of this simulation are constructed from an atmosphere with a GloSSAC aerosol profile and a layer of ice crystals between 12 km and 13 km. Simulated ALI observations are made, and then used in the albedo estimation to select the forward model albedo as would be done in a non-simulated application. This albedo informs θ of a simple Rayleigh atmosphere (no aerosol or ice) which constructs the a-priori profile. The atmospheric forward model is no longer used in the retrieval beyond this initial set-up stage. The simulated exercise is summarized in Fig. 7. Note that details of the cloud detection shown in (h) and (i) of Fig. 7 is discussed shortly in Section 4.2.3.

For all intents and purposes, this simulated retrieval produced results well representative of the true state. In this example θ received little to no action by the inversion to adjust it form the a-priori state. It is sensible to simply not include θ as a property in $\boldsymbol{x}$ and just rely on the a-priori values in the forward modelling. However, in practice we found it was helpful to include θ for application on the real measurements in Scans 1, 2, and 3 to match the measurement vectors. This may indicate left over instrument biases in the calibrated profiles that is not forward modelled correctly, or that the polarimetry of the real atmosphere is not captured as well by the constructed a-priori profiles as the prototyping indicated. In either case, we do not find this an impactful issue for the determination of cloud scattering tangent altitudes.

4.2.3 Cloud Identification from the DoP

We examine the well retrieved DoP shown in (d) of Fig. 7 to set a lower altitude limit of the aerosol retrieval. We use a simple edge detection algorithm after first smoothing the DoP (dots of (h) in Fig. 7) using a Savgol filter (producing the solid line of (h) in Fig. 7). Next we convolve the smoothed DoP with a central difference impulse response to identify a stark change

https://doi.org/10.5194/egusphere-2025-67
Preprint. Discussion started: 31 March 2025

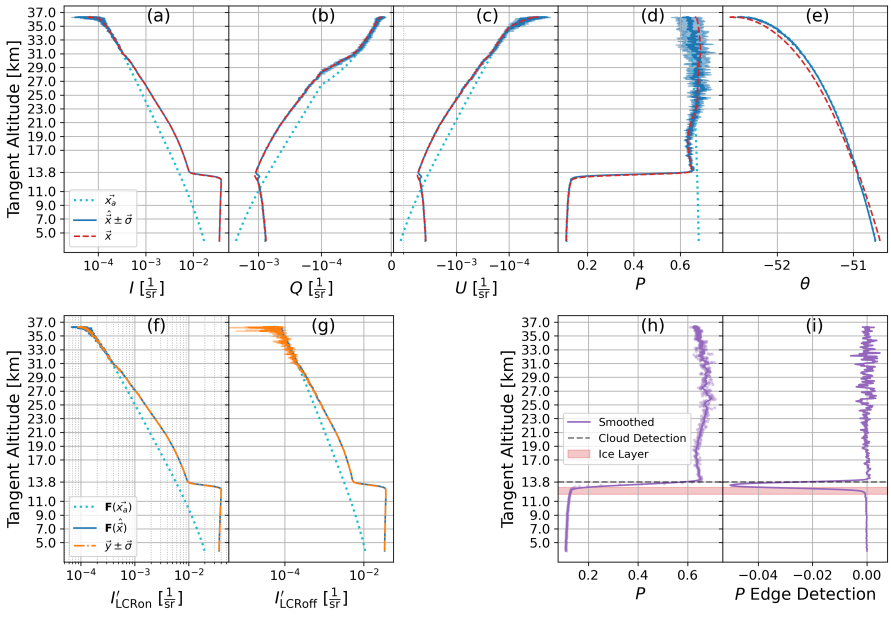

Figure 7. Summary of the atmospheric Stokes retrieval used for cloud discrimination using 1105 nm observations as an example. (a, b, c, d, e) The Stokes and Poincaré parameters of the atmospheric state, where $\boldsymbol{x_a}$ (dotted cyan) represents the a-priori state, $\boldsymbol{x}$ (solid blue) represents the final retrieved state, and $\hat{\boldsymbol{x}}$ (dashed red) represents the true state of the simulation. (f, g) The profiles of $\boldsymbol{y}$ where $\mathbf{F}$ represents the forward modelling profiles using Equations 10 and 11. (h, i) The demonstration of the cloud identification using a stark change in DoP as indication of cloud scattering.

in polarized behaviour. We take the higher altitude of the full-width half-max of the peak as the indication that the scattered signal is now contaminated with the presence of cloud. This process is demonstrated in (h) and (i) of Fig. 7, which arrived at an answer of 13.8 km. It is known form the true state of this simulated exercise that the depolarizing ice layer is just slightly below this at 12 km to 13km, thus making this a satisfactory indication.

A reader may wonder why the effort to retrieve the Stokes profiles of the atmosphere is justified if only an edge in the DoP is used to identify a cloud deck altitude, since one may expect that a very similar edge is also seen in the DoP approximation provided by Equations 5 to 7. While indeed the approximate measure of $\tilde{P}$ yields a similar answer for the example in Fig. 7, one needs to emphasise that the λ dependant non-ideal behaviour of the LCR affects the ability to do this. For example, Fig. 8 shows the DoP for the same exercise of Fig. 7 except now at 865 nm instead of 1105 nm, and with the inclusion of $\tilde{P}$ shown as the orange line. Referring to Equations 1, 10 and 11 the radiance profiles measured by ALI in the LCR on and off configurations depend on the combined response of the Mueller matrix of ALI, and that of the polarized state of light being observed. As the $\tilde{P}$ of Fig. 8 indicates, in this scenario the combined response at 865 nm comes close to looking identical between LCR on and LCR off measurements and yields a very small (and incorrect) DoP compared to that of the true state

https://doi.org/10.5194/egusphere-2025-67
Preprint. Discussion started: 31 March 2025

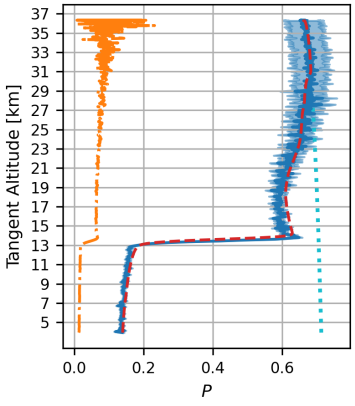

Figure 8. DoP retrieval (similar to plot to (d) of Fig. 7) at 865 nm. The a-priori DoP (dotted cyan) shown along with the true DoP of the simulation (dashed red) and the retrieved DoP (solid blue). The approximation of the DoP ($\tilde{P}$) made directly from ALI observations (Equation 5 to 7) is shown as the dashed-dot orange profile. The approximation gives a very small and incorrect profile, but the retrieval method yields a much more robust and correct result.

when directly approximated. However, the retrieval method is robust enough to still arrive at the true state and provide a better quantification of the DoP.

4.2.4 ALI DoP Limitations

While the retrieval method is more robust than the approximations of Equations 5 to 7, it is still limited. Observations of I'_{LCRoff} and I'_{LCRon} result from the combined wavelength dependent response of the non-ideal ALI Mueller matrices, and that of the polarized light in the atmosphere. The combined response can lead to similarity (at least at some wavelengths) between I'_{LCRoff} and I'_{LCRon} measurements that construct $\boldsymbol{y}(\lambda)$ of the retrieval through Equations 8, 10 and 11. If these measurements are similar than polarization cannot be distinguished.

We demonstrate this in simulation where the geometry and solar conditions of each scan of Table 1 is used and the DoP is retrieved. At each scan, the true state of the atmosphere includes GloSSAC aerosol but unlike the exercise of Fig. 7 and Fig. 8 no ice layer is included. Otherwise, the approach is the same as already discussed. This simulation is run twice, once with the polarimetric response of ALI, and again with an “ideal ALI" behaving as a perfect vertical or horizontal polarizer for each respective LCR state. We show the results in Fig. 9.

As these results show, when ALI behaves as ideal linear polarizers the DoP retrievals of all three scans ((f, g, h) of Fig. 9) fall well within 5% of the true state DoP values. This is because there is no practical potential of LCR on and off measurements looking similar and the atmospheric DoP can be well resolved. However, the non-ideal behaviour of the LCR (particularly in the off state) causes ambiguity for Scan 1 and Scan 3 shown in (b) and (d) of Fig. 9. Here the ambiguity manifested at the shorter wavelengths of Scan 1 and gave a nearly fully polarized DoP retrieval, where as Scan 3 the ambiguity at the longer wavelengths

https://doi.org/10.5194/egusphere-2025-67
Preprint. Discussion started: 31 March 2025

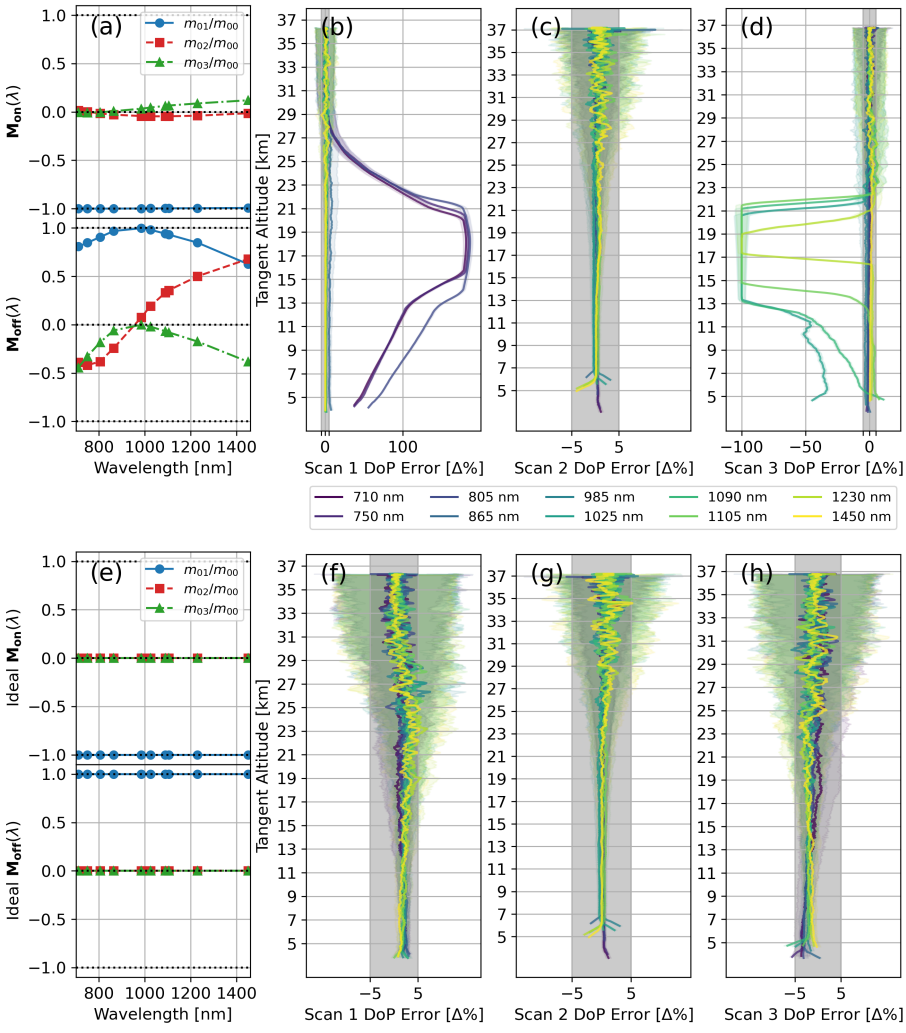

Figure 9. Error of DoP retrievals against the combined response of the ALI Mueller matrix and the simulated atmospheric Stokes for all three scans of Table 1. (a) The ALI Mueller matrix coefficients for LCR on and off states (same Mueller response shown in Fig. 3). (b, c, d) The error in the DoP retrieval as a percent change from the known true state of the simulation using the response in (a) for Scan 1, Scan 2, and Scan 3 respectively. (e) Ideal Mueller coefficients for LCR on and off states. (f, g, h) The error in the DoP retrieval as a percent change from the known true state of the simulation using the response in (e) for Scan 1, Scan 2, and Scan 3 respectively. Results at different wavelengths shown by the coloured lines in (b, c, d, f, g, h) with the shaded regions indicate one sigma of uncertainty in the retrieved DoP profile.

yielded an almost completely randomly polarized atmosphere. However, in Scan 2 (shown in (c) of Fig. 9) the atmospheric Stokes parameters being measured by ALI did not produce ambiguity after transformation by the Mueller matrices, and the DoP is still resolved at all wavelengths.

https://doi.org/10.5194/egusphere-2025-67
Preprint. Discussion started: 31 March 2025

4.3 Aerosol Retrieval

In this section we discuss the performance of the ALI aerosol retrievals in simulation against known true state aerosol. We would again like to emphasise that the in the context of the present work, the algorithmic criteria we set is to retrieve an altitude resolved unimodal log-normal aerosol population, where both the altitudinal number density and median radius are retrieved along side a scalar width. To begin, we define the state vector of the aerosol retrieval to be the vertically resolved number density N (units of cm^{-3}), and median radius r (units of $\mu\mathrm{m}$) of a unimodal log-normal aerosol profile. Unless explicitly noted otherwise, the width w of this log-normal distribution is also retrieved, but only as a single scalar value which is applied to all altitudes. In prototyping, an effort was made to retrieve a vertically resolved width profile along with the number density and median radius. However, we found that while the true state aerosol extinction was well retrieved, their is simply too much freedom in the state solution space to arrive at any viably robust solution of the state properties themselves from ALI measurements. This is an unsurprising conclusion given other similar efforts (Rieger et al., 2014; Malinina et al., 2018). Therefore, we limit our retrieval state vector $\boldsymbol{x}$ to just the properties of N, r and (scalar) w as:

$$\boldsymbol{x} = \begin{bmatrix} N_{\text{low alt}} & \dots & N_{\text{high alt}} & r_{\text{low alt}} & \dots & r_{\text{high alt}} & w \end{bmatrix}^T \tag{12}$$

where the lowest altitude is determined by the lowest observed tangent altitude not considered contaminated by cloud scattering as discussed in Section 4.2. As for the high altitude limit, as Table 1 indicates the gondola of the example science scans was at a float altitude between 36 km and 37 km, which allows for the possibility of retrieving nearly up to these altitudes. However aerosol number density can be very small at altitudes above 30 km, and results from prototyping our retrieval algorithm showed that retrieving aerosol where the density approaches zero yields very large uncertainties in the median radius. Therefore, for the context of the present work we generally select 30 km as the ceiling of the retrieved state vector. Due to this, we also limit the ceiling on of the radiance profile which construct $\boldsymbol{y}$ at this altitude as well.

Of note, in our forward modelling SASKTRAN calculates the radiative transfer for altitudes between 0.5 km to 45 km at 500 orders of scatter. The aerosol outside of the actively retrieved altitudes is scaled for altitudes below the lower altitude limit, and fixed to be zero in number density above the retrieval ceiling. Furthermore, in our retrieval the vertical resolution of the state vector is effectively set by the resolution of the altitude grid in SASKTRAN. We set the discrete altitude grid of SASKTRAN to be 0.5 km to 45 km in steps of 0.6 km, where the 0.6 km resolution was determined as the finest resolution $\mathbf{A}$ produced given the content of the $\boldsymbol{y}$ we employ.

Given we do not employ regularization, we then construct $\mathbf{S_a}$ as a diagonal matrix with selected variances. For the number density state we select the a-priori variance such that the retrieval is stabilized in the high-altitude region where the aerosol number density is small, as well as the SNR of $\boldsymbol{y}$ being relatively smaller (providing poorer conditions for the inversion to work at these altitudes). Table 3 shows the variances we use along the diagonal of $\mathbf{S_a}$ corresponding to the number density state property and its altitude. The a-priori variance of the median radius is made uniform with respect to altitude and selected to be 0.01. The scalar width has this variance set to 0.0001.

https://doi.org/10.5194/egusphere-2025-67
Preprint. Discussion started: 31 March 2025

Table 3. Diagonal a-priori covariance values

Altitude m	5500.0	10000.0	22500.0	30000
Number Density Variance	200	100	10	0.2

A-priori variance used to construct the diagonal elements of $\mathbf{S_a}$ corresponding to number density. Values are specified against SASKTRAN altitude, and are interpolated onto the forward modelling grid.

The measurement vectors $\boldsymbol{y}$ are simply stacked vertical radiance profiles, with $\mathbf{S}_\epsilon$ constructed as a diagonal matrix containing the variances associated with each element of $\boldsymbol{y}$. No processing is done to the measurements of $\boldsymbol{y}$ for the sake of the inversion beyond truncating the tangent altitudes to only the region between the low-altitude and high-altitude cut-off, and high-altitude normalization. High-altitude normalization is done primarily to compensate for albedo affects which are not well encapsulated by forward model using the values determined in Table 2. The normalization itself is done by dividing by the mean signal level of each radiance profile between the tangent altitudes of 30 km and 33 km. The error associated with each point of the profile is then scaled to conserve the relative SNR at each tangent altitude of the measurement.

Additionally, while a full science scan of ALI consists of the of the 10 wavelengths mentioned in Section 3 in both LCR on and off states we have chosen not to use them all here. In the context of the present work we focus on using the measurements provided by the on wavelengths of 750 nm , 1025 nm , and 1230 nm of the LCR on state. The reason for this restriction is that including the other wavelengths and LCR states (or the Stokes parameters of Section 4.2) within $\boldsymbol{y}$ did very little to increase the information content of the retrieval in prototyping, at least within the scope of our approach of retrieving a unimodal log-normal aerosol distribution. Furthermore, as mentioned before the other wavelengths can introduce further complexity as the wings of the ATOF bandpass have sensitivity to trace gas absorption which needs further and careful analysis to handle.

The dampening matrix $\mathbf{D}$ is constructed similar to the dampening matrix discussed in the context of Section 4.2, that is we construct $\mathbf{D}$ in state space as a diagonal matrix populated with the diagonal values of $\mathbf{K}^T\mathbf{S}_\epsilon\mathbf{K}$. However, unlike Section 4.2 the dampening matrix is not further configured. This matrix is paired with a starting γ of 1.0 which is adjusted according to the minimization of the cost function.

4.3.1 Aerosol Retrieval Simulations

We now present a summary of retrieval result obtained in pure simulation where the true state aerosol is known. In these simulations we construct the true state aerosol profile from GloSSAC extinctions for realistic aerosol scattering, and use the geometry provided in Scan 3. For this true state aerosol, we customize r and w, and then adjust N such that the GloSSAC extinction is conserved at 525 nm. The main exception to this conservation of GloSSAC extinction is we force the true state number density above 30 km to be zero. We do this because of our use of high-altitude normalization, which makes this assumption implicit.

https://doi.org/10.5194/egusphere-2025-67
Preprint. Discussion started: 31 March 2025

First we will show a simplified case of our standard retrieval approach in which only the vertical profile of N and r is retrieved. In this specific exercise w is fixed at what normally is our a-priori value of 1.6 for both the true state and the retrieval forward modelling. We also choose for our a-priori and initial state a uniform r of 0.08 μm, and an a-priori N profile which is shown alongside our exercises. However, of note this a-priori N profile is not constructed from any specific knowledge of the aerosol to be retrieved, and these a-priori values are used in all exercises (real and simulated) for the remainder of the present work. This retrieval is shown in Fig. 10 where the GloSSAC aerosol extinction is obtained by retrieving a N and r profile, both of which are well representative of the true state parameters.

Now we demonstrate the efficacy when the retrieval of Fig. 10 is repeated, but with the addition of the scalar w re-included in $\boldsymbol{x}$ as our nominal approach uses. The true state width is made scalar at 1.5. The state results are shown in Fig. 11. This simulation represents the *viable* limits of our approach. Note that while the true state extinction is well retrieved and $\boldsymbol{y}$ is well agreed, the scalar width was unable to obtain the correct value despite the true state width also being scalar. Furthermore, the shape of both the N and r states is is well represented and only separated from the true state by the biased caused by the incorrect retrieval of w. Essentially the retrieval found an aerosol particle size and number density which reproduces the ALI observations while not being faithful of the true state. Despite this however, the retrieved w is still an improvement over our a-priori w, and because of this we consider this a better retrieval approach over assuming a fixed width.

Our final two simulations we present shows the behaviour of the algorithm in the presence of more complex aerosol distributions - which we present to contextualize some results in Section 5. In this exercise the ground truth aerosol is bimodal with N, r, and w all varying in altitude. We then apply our retrieval algorithm assuming a unimodal distribution with a scalar w in two cases. The first case uses the observational and solar geometry of Scan 3 (as the retrievals of both Fig. 10 and Fig. 11 used), where the polarization of limb-scattered sunlight is expected be horizontally dominated. The second case uses the solar geometry of Scan 1, where the limb viewing geometry is expected to yield a *relatively* equal balance between horizontal and vertically polarized light.

The results of the first case using Scan 3 geometry is shown in Fig. 12. It is rather clear that the retrieval algorithm we present fails to arrive at a representative atmospheric state which can well reproduce all of the ALI observations of the more complex aerosol. In particular, the retrieved extinction underestimates the total true state extinction of the bimodal distribution shown as the red line in Fig. 12. For clarity, the inversion itself worked as intended but was unable to produce a more optimized $\boldsymbol{x}$ than what is shown under these conditions. However, when we repeat the retrieval of the exact same bimodal distribution - changing only the geometry to that of Scan 1 - the results shown in Fig. 13 are obtained. While there are still inaccuracies of this retrieval, particularly in the reproduction of $\boldsymbol{y}$ using the retrieved representative unimodal distribution, the overall performance significantly improved over using the geometry of Scan 3. Of particular note, the retrieved extinction very well represents the true state of the bimodal distribution.

We wish to emphasize that the limb measurements of ALI are polarized, and we speculate that this polarized content contains useful information about the aerosol phase scattering matrices - which is of course influenced by the particle sizes. The more the limb-scattered radiance is polarized the more pronounced the requirement of accurately modelling the aerosol scattering matrices is. This may yield potential to retrieve more complex aerosol distributions with more complex retrieval approaches.

https://doi.org/10.5194/egusphere-2025-67
Preprint. Discussion started: 31 March 2025

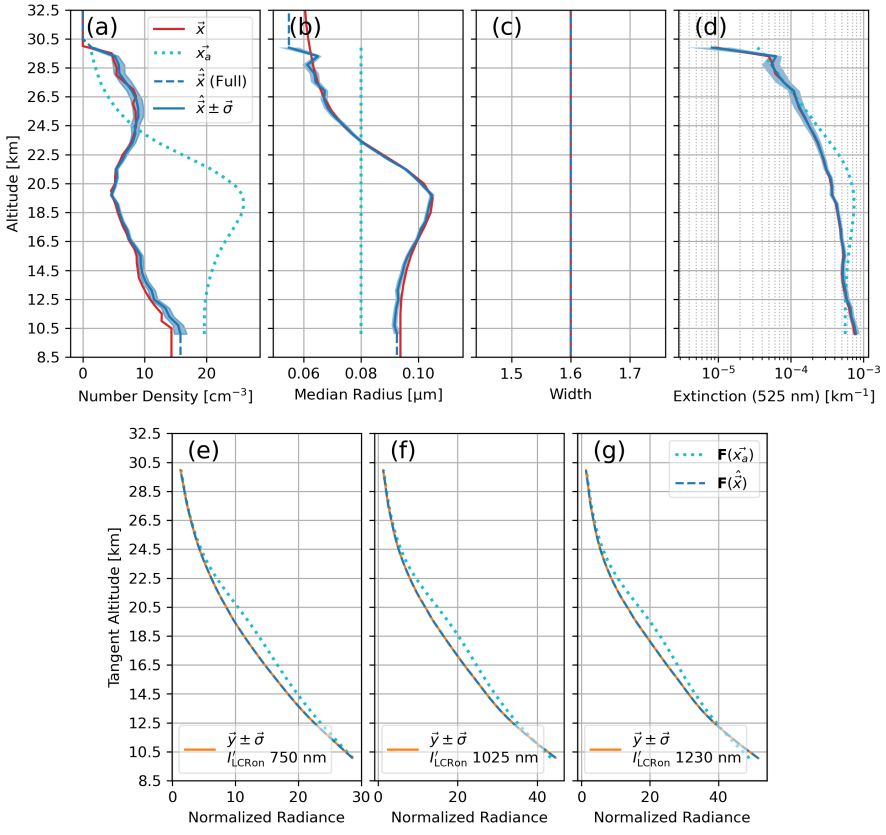

Figure 10. Simulated ALI unimodal log-normal aerosol retrieval under a simplified approach which fixes the aerosol distribution width at 1.6. (a) Profile of aerosol number density. (b) Profile of aerosol log-normal median radius. (c) Profile of aerosol log-normal width. (d) Profile of aerosol extinction. In (a,b,c,d) the red lines represent the true state of the simulation, and the cyan dots show the a-priori and initial state of the retrieval. The dashed blue lines show the state being modelled in SASKTRAN outside of our active retrieval altitudes, while the solid blue line shows the retrieval itself. Note that the blue shaded region represents 1 standard deviation of uncertainty for retrieved each state. (e) Measurement vector of 750 nm. (f) Measurement vector of 1025 nm. (g) Measurement vector of 1230 nm. In (e, f, g) all profiles are from LCR on observations. The cyan dotted line is the forward modelled vector given the a-priori state, the dashed blue line is the forward modelled vector of the final retrieved state, and the orange line is the actual vector made form ALI observation (simulated from the true state atmosphere). Error bars of the measurement are shown, but too small to be easily visible. This small error primarily results from the horizontal averaging.

However this is a point of on-going research and not within current scope. The relevant conclusion to be made from the results of Fig. 12 and Fig. 13 is that through prototyping our algorithm, we expect a unimodal distribution to be more representative of a complex aerosol population the less polarized the observations are.

https://doi.org/10.5194/egusphere-2025-67
Preprint. Discussion started: 31 March 2025

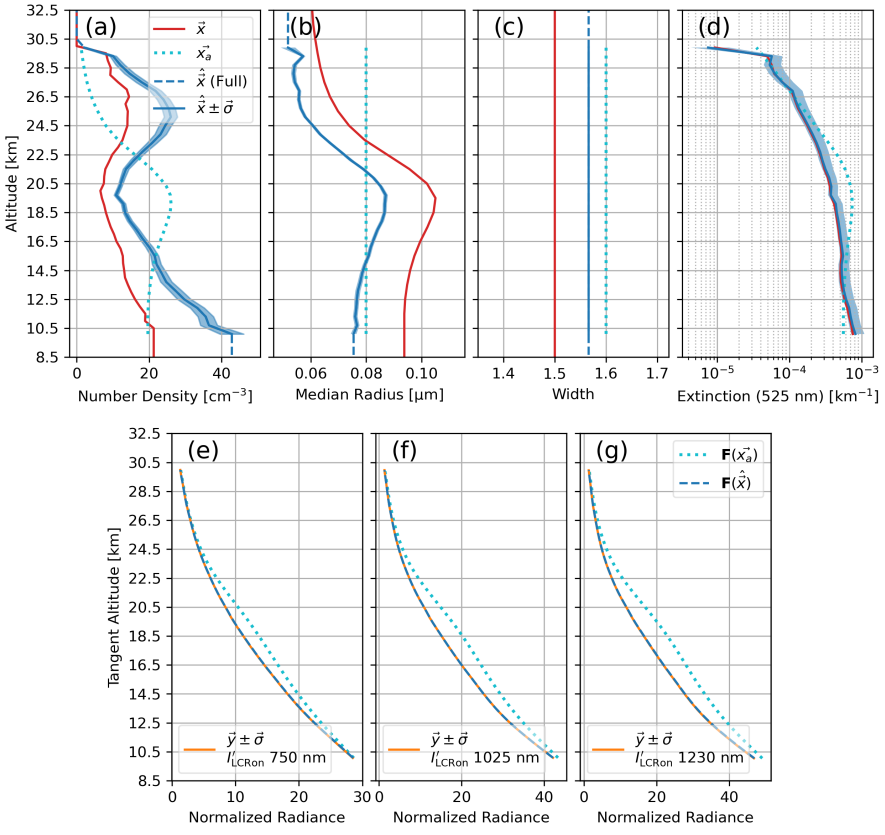

Figure 11. The unimodal log-normal aerosol retrieval of Fig. 10 but now retrieving the width (our nominal approach). Descriptions of (a, b, c, d, e, f, g) same as Fig. 10. Important here is the measurement vectors and aerosol extinction profile agree well, but the retrieved N, r, and w are biased from the true state. The retrieval has determined a different aerosol population which still reproduces the ALI observations.

5 Aerosol Retrievals of the Flight Campaign

With efficacy of our approach evaluated in Section 4, we now show its application to the exemplar ALI observations summarized in Table 1 made during the last high-altitude balloon flight. We begin with the cloud discrimination by retrieval of the DoP profiles, shown for all three scans in Fig. 14. From this analysis, cloud contamination begins at a tangent altitude of 10.8 km in Scan 1 and 10.2 km in Scan 2. As expected from the example image of Scan 3 in Fig. 5, it did not produce a change in the DoP profile that would indicate the presence of significant cloud. For the purposes of this scan we simply select a lower limit of 10 km only for consistency with Scan 1 and 2.

Furthermore, as mentioned before we note that Scan 3 is the noticeably more polarized than Scan 1 or 2, and Scan 1 is the least polarized. With respect to the simulations done in the exercise surrounding Fig. 9, we find almost all behaviour regarding Fig. 14 to be expected including: the relative balance between horizontal and vertical polarizations for all three scans, the

https://doi.org/10.5194/egusphere-2025-67
Preprint. Discussion started: 31 March 2025

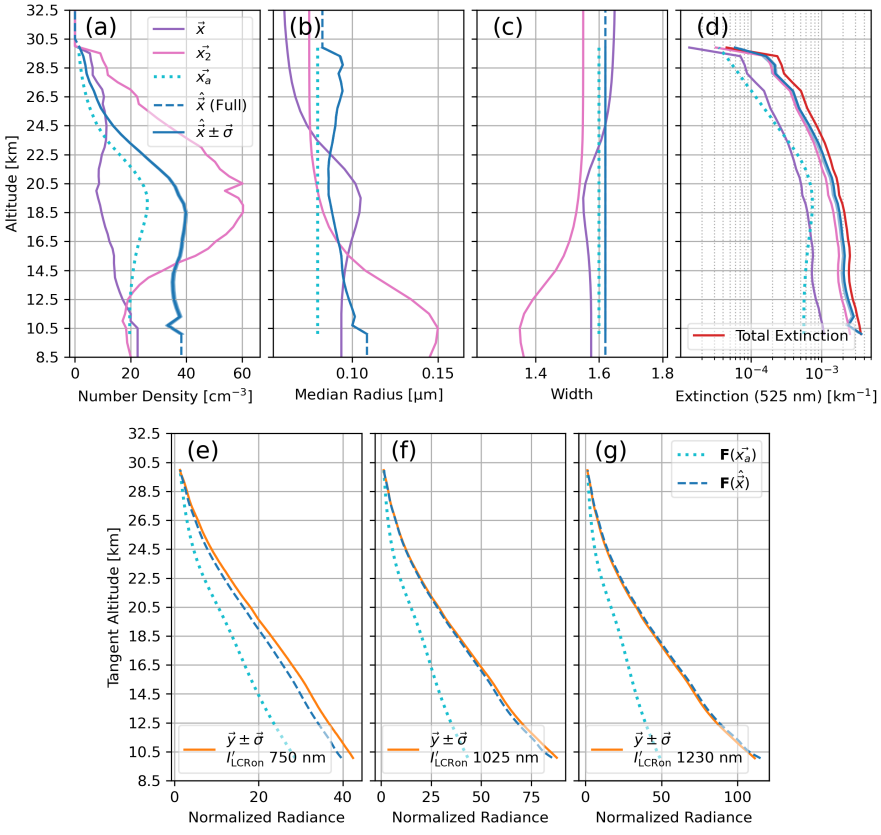

Figure 12. Unimodal aerosol retrieval algorithm performance under observation of a bimodal distribution using the geometry of Scan 3. The solar scattering angles of Scan 3 are expected to give horizontally dominated limb-scattered radiance. Descriptions of (a, b, c, d, e, f, g) same as Fig. 10, except (a, b, c, d) now show the true state of the bimodal distribution in purple and pink.

spectral regions expected to fail given the polarimetric response of ALI in Scan 1 and Scan 3, and the relative magnitude of the DoP for Scan 1 and Scan 2. However, a notable exception to our expectations is the magnitude of the retrieved DoP in Scan 3 of Fig. 14. The simulation of this geometry done for Fig. 9 produced a true state DoP approximately ranging between 0.3 - 0.4, but the corresponding DoP in Fig. 14 is significantly larger. We find no indication that these results are erroneous and consider that the increased DoP is a measured feature of the atmosphere, but the cause is still under investigation.

As we apply our retrieval approach to each scan, we compare our results to the extinction of three other instruments: SAGE III, OMPS, and OSIRIS. In this comparison, we convert our unimodal log-normal state parameters to an extinction at 750 nm for relevant comparison. However, to first establish the initial footing of this comparison we begin by simplifying the retrieval approach we have discussed in Section 4.3, and apply only our 750 nm measurements to retrievals with fixed r of 0.08 $\mu\mathrm{m}$ and fixed w of 1.6. This is a similar approach to the standard retrieval approach of OSIRIS and OMPS (Rieger et al., 2019; Taha et al., 2021). In this simpler retrieval only N is adjusted in $\boldsymbol{x}$ such that we arrive at an aerosol extinction directly retrieved

https://doi.org/10.5194/egusphere-2025-67
Preprint. Discussion started: 31 March 2025

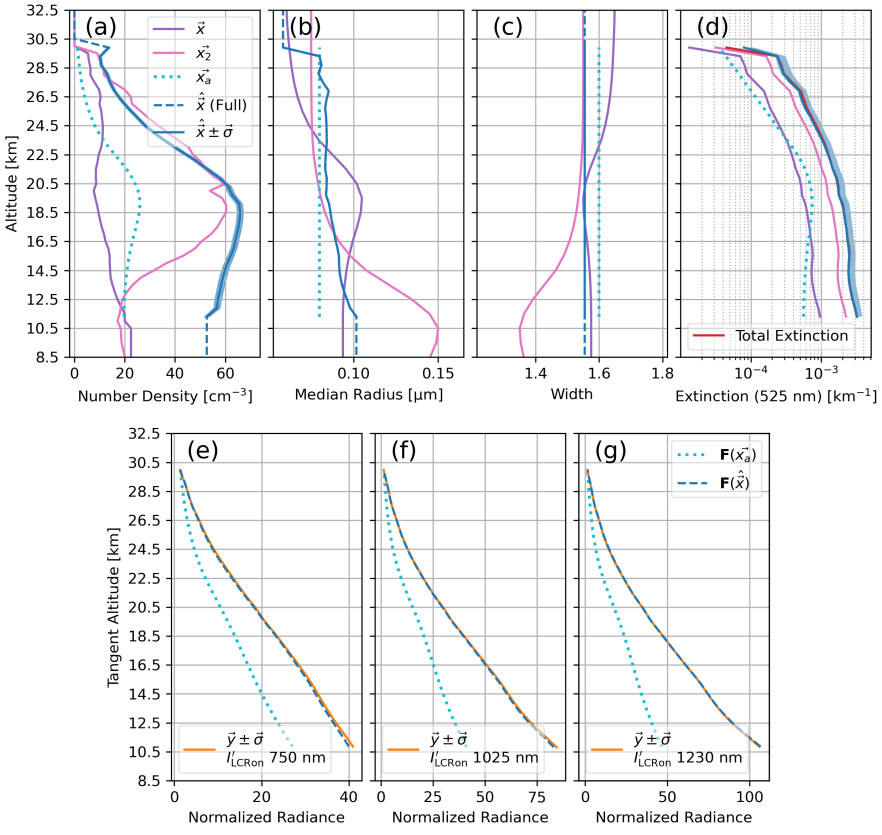

Figure 13. Retrieval of Fig. 12 repeated using the geometry of Scan 1. Descriptions of (a, b, c, d, e, f, g) same as Fig. 12. The solar geometry of Scan 1 is expected to yield a generally neutral balance between vertically and horizontally polarized limb-scattered light. With respect to Fig. 12, the change in geometry leading to a less polarized observation allowed the unimodal assumption to perform better.

at 750 nm. Since the observations of ALI are polarized, we attempt to compensate in this simplified retrieval by constructing $\boldsymbol{y}$ using a 750 nm Stokes parameter I profile built with the approximation of Equation 5. We use $\tilde{I}$ since the retrieval of I used in the cloud discrimination is not available for Scan 1. Note however that in this retrieval, the forward modelling of ALI observations is still all polarized appropriate to the ALI flight observations being used. Figure 15 shows the results of this extinction exercise. Retrieving extinction at only 750 nm yields respectable agreement overall for all three scans. We note however that with respect to the other instruments, our retrievals tend to over estimate the extinction in the lower altitudes.

We now show our algorithm which retrieves N, r, and a scalar w using the LCR on measurements of 750 nm, 1025 nm, and 1230 nm of ALI applied to all three scans of Table 1. Beginning with the retrieval of our nominal scan, Scan 1 shown in Fig. 16, shows a fairly ideal retrieval. All three measurement vectors produced by the retrieved aerosol state agree very well to the ALI observation of the flight, and the retrieved extinction well represents the extinction profile of all three comparison instruments. We note that the lower altitude bias of ALI with respect to the other three instruments seen in Fig. 15 is largely

https://doi.org/10.5194/egusphere-2025-67
Preprint. Discussion started: 31 March 2025

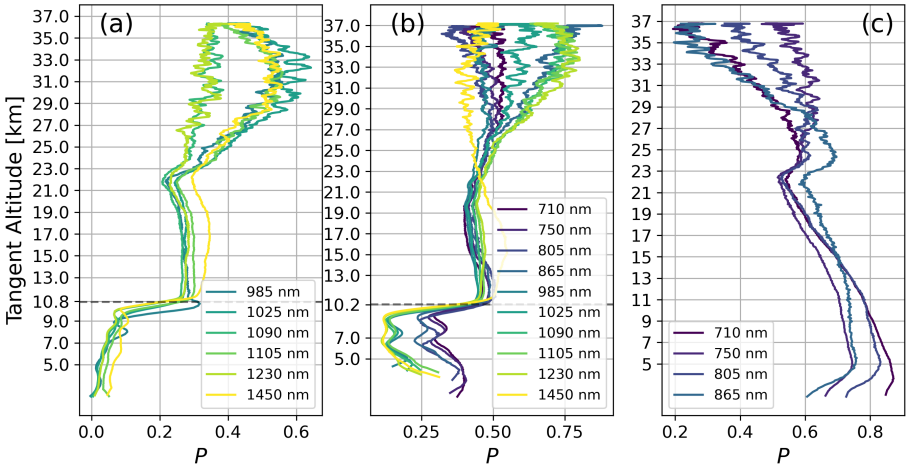

Figure 14. DoP profiles of all three scans found following the technique shown in Section 4.2. (a) Results of Scan 1. (b) Results of Scan 2. (c) Results of Scan 3 (no significant cloud). Dashed black line indicates the tangent altitude of cloud contamination. Coloured lines show analysis at different wavelengths. Wavelengths not shown were too similar between LCR on and LCR off states of ALI to distinguish atmospheric polarization.

brought into agreement. Additionally, the w of this retrieval did not adjust significantly from the a-priori value of 1.6, however of interest is the profile of r which indicates a layer of larger particles at approximately 22.5 km.

The retrievals of Scan 2 and Scan 3, shown in Fig. 17 and Fig. 18 respectively, maintain larger disagreement with OMPS, SAGE III, and OSIRIS than Scan 1. However, we also observe increased disagreement between ALI radiance in these two scans with respect to the forward modelled observations produced by the retrieved aerosol state. In particular, the measurement vector of 750 nm in Scan 2 has large disagreement with the ALI measurement. Furthermore, all three measurement vectors of Scan 3 show inconsistencies similar to that observed in the simulated exercise of Fig. 12.

We recognize the possibility that errors such as: uncertainties in the attitude solution of the gondola, instrumentation biases not correctly removed during calibrations, or aspects of the atmosphere external to aerosol which have not been properly accounted for in the forward modelling could also exhibit themselves as the disagreements shown in Fig. 17 and Fig. 18. However, we find no significant reason to suspect these possibilities above the explanation provided by the bimodal exercise of Section 4.3. In pure simulation where observational geometry and forward modelling are identical between simulated observations and the inversion process, we demonstrated the creation of a similar retrieval disagreement in our approach when it is applied to more complex aerosol distributions than the retrieval assumes. This disagreement is mitigated as only the geometry is changed from Scan 3 to Scan 1, where the limb-scattering conditions produce a less polarized atmosphere. We consider that the relatively good performance of Scan 1 in Fig. 16 with respect to Scan 3 in Fig. 18 is an indication that the affect discussed in Section 4.3 related to this is manifesting.

With that said, we can also highlight positive aspects of the Scan 2 and Scan 3 retrievals. As indicated by Table 1 Scan 1 and Scan 3 are both looking south, so they should be observing very similar aerosol. We see this represented in the similar shapes

https://doi.org/10.5194/egusphere-2025-67
Preprint. Discussion started: 31 March 2025

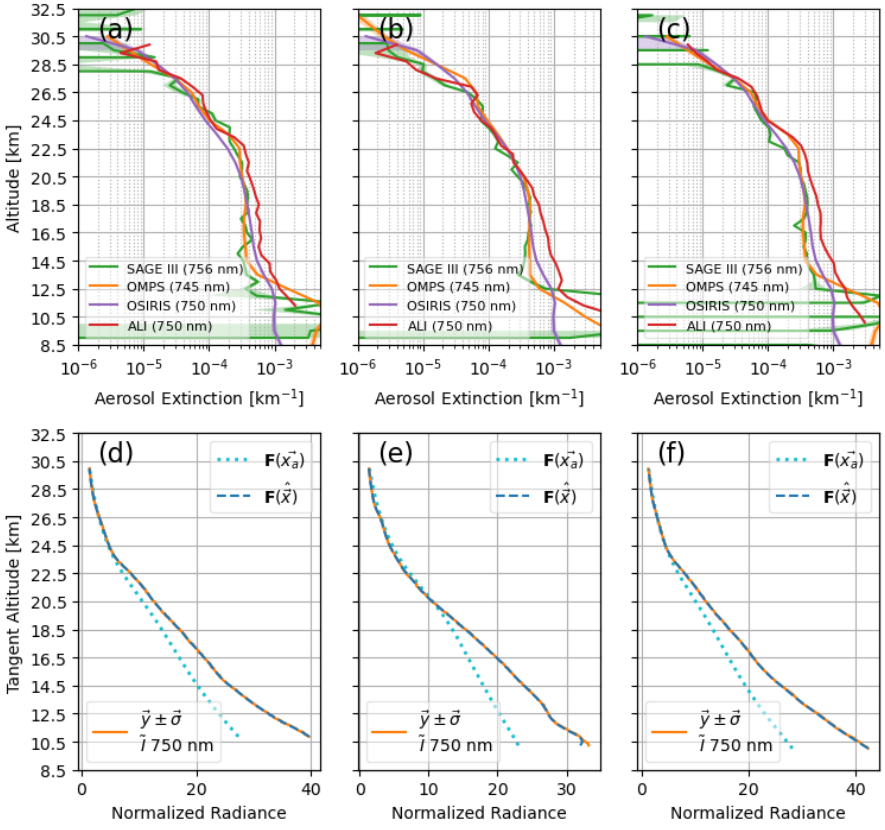

Figure 15. Extinction retrievals from each ALI scan using only $\tilde{I}$(750 nm) built with Equation 5 compared against extinction profiles of SAGE III, OMPS, and OSIRIS. (a) Extinction retrieval of Scan 1. (b) Extinction retrieval of Scan 2. (c) Extinction retrieval of Scan 3. (d) ALI measurement vector corresponding to extinction retrieval of Scan 1. (e) ALI measurement vector corresponding to extinction retrieval of Scan 2. (f) ALI measurement vector corresponding to extinction retrieval of Scan 3. In (d,e,f) the cyan dotted line is the forward modelling of the measurement vector given the a-priori state, the dashed blue line is the forward modelled measurement vector of the final retrieved state, and the orange line is the actual measurement vector made form ALI observation.

of the states between these two scans - in particular the r profiles. However, we also note that in Scan 3 r at lower altitudes gets significantly smaller than in Scan 1, while N increases significantly. We speculate that this is another manifestation of the retrieval trying to optimize a unimodal distribution to match the polarized $\boldsymbol{y}$ produced by a more complicated aerosol population. In contrast, the retrieved state of Scan 2, which is looking north, is yielding a distinctly different radius profile. This indicates that even under the limitations of our approach, the retrievals are still sensitive to aerosol particle size information. Additionally, we highlight that the overestimation of aerosol extinction with respect to SAGE III, OMPS, and OSIRIS seen in Scan 2 and Scan 3 is similar to what was seen in the more straightforward 750 nm extinction retrievals shown in Fig. 15. Except unlike the simplified retrievals there is now the indication of a biased state given the $\boldsymbol{y}$ disagreement with our approach.

https://doi.org/10.5194/egusphere-2025-67
Preprint. Discussion started: 31 March 2025

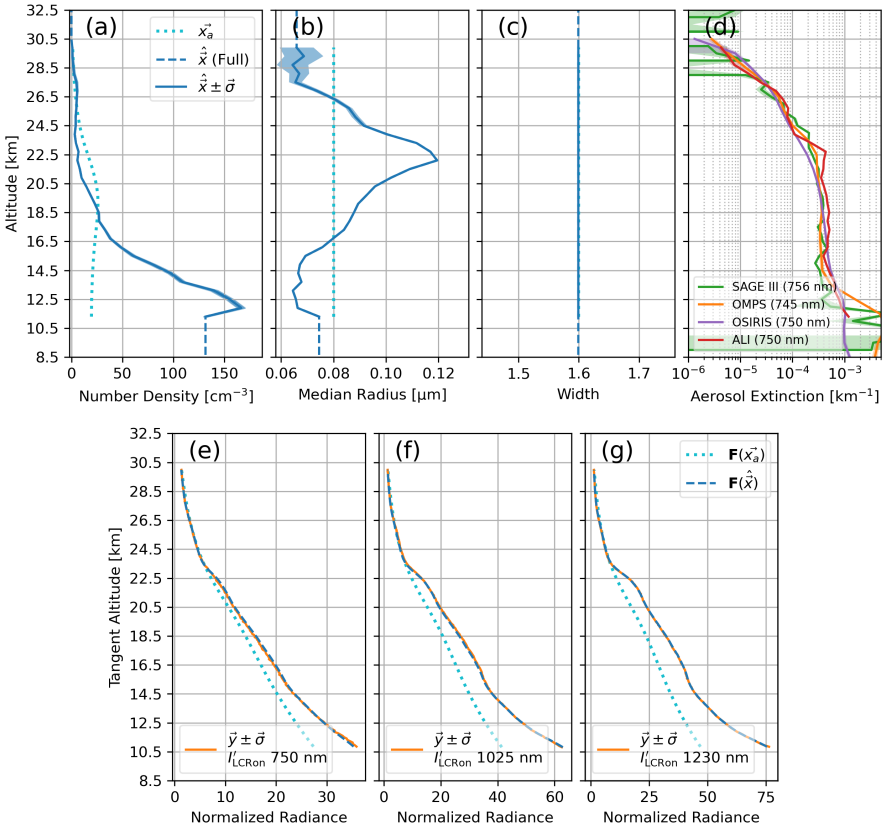

Figure 16. Aerosol retrieval of Scan 1 (nominal conditions). (a) Profile of retrieved aerosol number density. (b) Profile of retrieved median radius. (c) Retrieval of scalar width. (d) Retrieved aerosol extinction profile of ALI shown with SAGE III, OMPS, and OSIRIS. (e, f, g) Retrieval measurement vectors as described in Fig. 10, noting that the orange is now made from ALI flight observation. The aerosol properties retrieved by ALI measurements produces an extinction profile in agreement with SAGE III, OMPS, and OSIRIS extinction.

6 Conclusions

We presented the atmospheric aerosol profiling capabilities of ALI which comprises two central aspects: retrieval of the atmospheric DoP to determine influence of cloud-scattered radiance, and a unimodal log-normal aerosol retrieval algorithm which employees the polarized radiance profiles ALI observes. The efficacy of both aspects was demonstrated in pure simulation with known true states. We find that the atmospheric DoP can be well retrieved, provided the combined response of the atmospheric Stokes parameters and the ALI Mueller matrix of LCR on and off states gives enough information to distinguish linear polarization. In this work we apply the DoP information to determine quantitatively a lower altitude limit of the aerosol retrieval which avoids cloud contamination.

https://doi.org/10.5194/egusphere-2025-67
Preprint. Discussion started: 31 March 2025

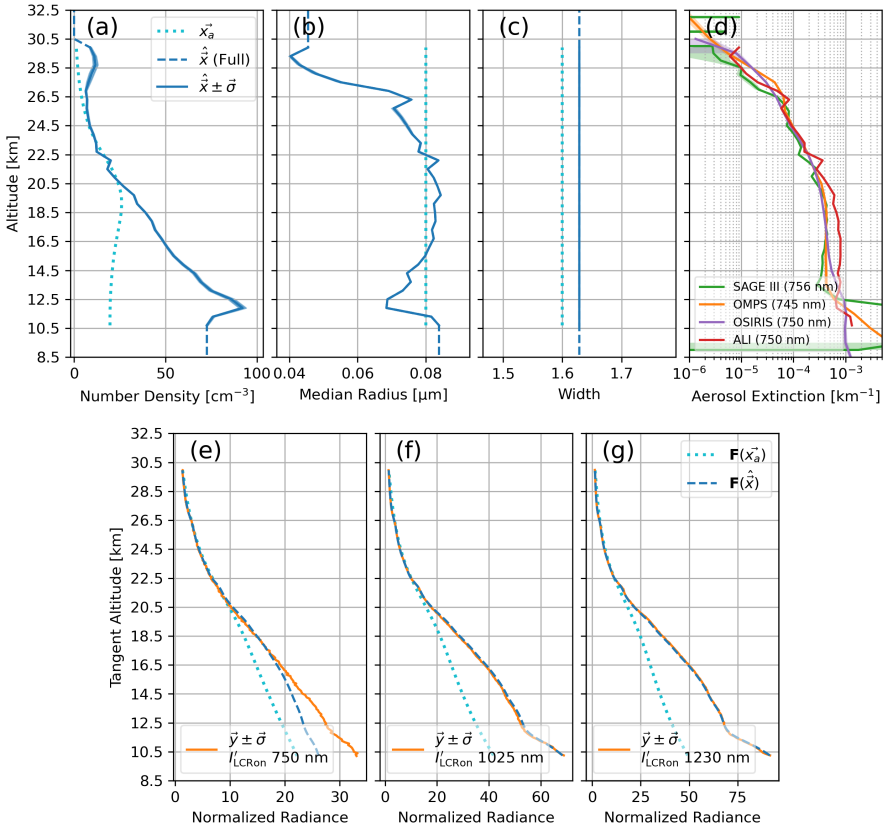

Figure 17. Aerosol retrieval of Scan 2 (vertically dominate polarization). Descriptions of (a, b, c, d, e, f, g) same as Fig. 16. Compared with the retrieval done for Scan 1, there is increased disagreement between the ALI extinction profile in (d), and that of SAGE III, OMPS, and OSIRIS. However, (e, f, g) also show increased disagreement between the forward modelled measurement vectors of the retrieved state and the flight observations of ALI. We suspect the unimodal assumption of the retrieved aerosol state is less able to perform under increasingly polarized conditions as discussed in the simulated exercise surrounding Fig. 12 and Fig. 13.

The unimodal log-normal aerosol retrieval itself retrieves aerosol number density. median radius, and a scalar width (applied to all altitudes of the distribution). While we find limitations to this technique which we discuss in Section 4.3, we see good performance when the assumption of a unimodal aerosol distribution is true. When a bimodal aerosol distribution is present under a unimodal assumption, we find the performance of our retrieval algorithm worsens as the polarization of the atmosphere increases. We speculate that the polarized radiance profiles of ALI contain useful information relating to the phase scattering matrices of the aerosol population, and as the atmosphere becomes more polarized the importance of accurately forward modelling the phase matrices (i.e. particle size) increases, and the more the unimodal assumption breaks down. This indicates further potential to retrieve more complex aerosol distributions using ALI observations with a more sophisticated retrieval algorithm, but we this is a point of our on-going research.

https://doi.org/10.5194/egusphere-2025-67
Preprint. Discussion started: 31 March 2025

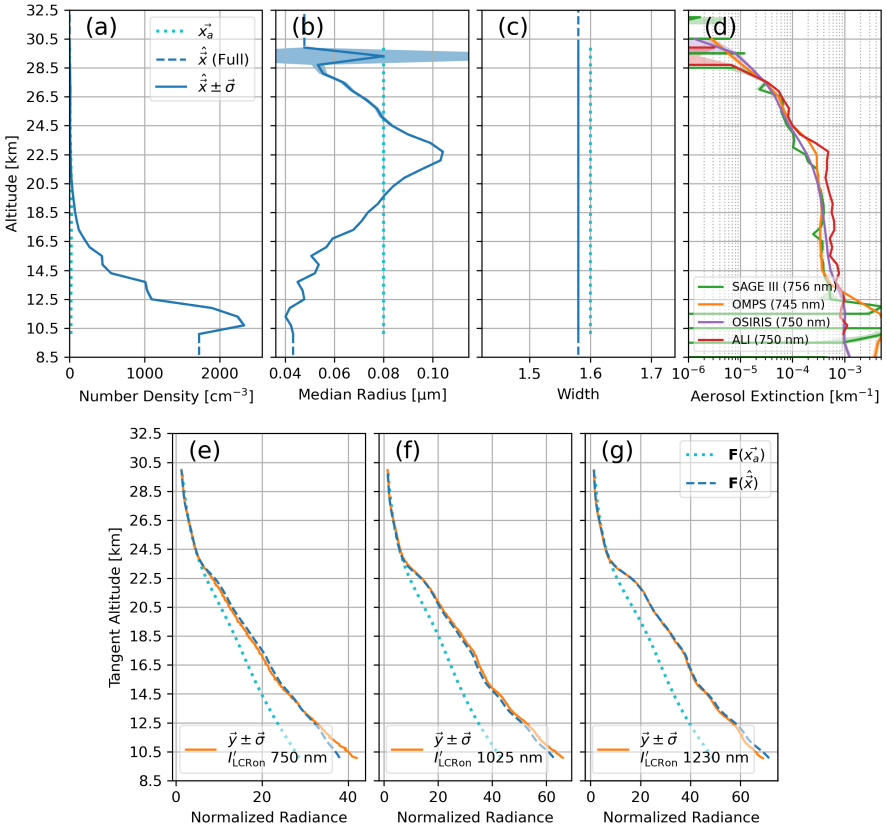

Figure 18. Aerosol retrieval of Scan 3 (horizontally dominate polarization). Descriptions of (a, b, c, d, e, f, g) same as Fig. 16. Similar to the Scan 2 retrieval, we again see increased disagreement with respect to the retrieval of Scan 1, and suspect the same root cause.

We conclude by applying our algorithm to retrieve the atmospheric aerosol observed by ALI during a high-altitude balloon flight in August of 2022. The results of three distinct sets (Scan 1, Scan 2, and Scan 3) of ALI observations are compared to the nearest coincident aerosol extinction profiles of SAGE III, OMPS, and OSIRIS. We find in this study that our nominal observations of Scan 1 produced a retrieved aerosol extinction in very good agreement to all three other instruments. Furthermore, the polarized retrieval of ALI yielded particle size information about the aerosol population in addition to the extinction. Scan 2 and Scan 3 showed an overestimation of aerosol extinction with respect to SAGE III, OMPS, and OSIRIS. However, the disagreement of these two scans can potentially be explained by the affect of using a unimodal distribution to represent more complex aerosol as seen the simulations. Supporting this statement is the relative improvement in the quality Scan 1 exhibits which is also replicated in simulation under this cause.

Data availability. Available upon request

https://doi.org/10.5194/egusphere-2025-67
Preprint. Discussion started: 31 March 2025

Author contribution. AB and DD are the heads of ALI project. DL, LG, and PL designed and built this ALI instrument. NL and LR gave software contributions. DL developed and performed data analysis. DL wrote manuscript draft. AB and DD reviewed and edited the manuscript.

Competing interests. The authors declare that they have no conflict of interest.

https://doi.org/10.5194/egusphere-2025-67
Preprint. Discussion started: 31 March 2025

References

Bass, M. and et al: Handbook of Optics: Volume I - Geometrical and Physical Optics, Polarized Light, Components and Instruments, McGraw-Hill Professional, New York, 3 edn., 2010.

Becker, A.: Kalman Filter from the Ground Up, https://www.kalmanfilter.net/book.html, 2023.

Bourassa, A., Degenstein, D., and Llewellyn, E.: SASKTRAN: A spherical geometry radiative transfer code for efficient estimation of limb scattered sunlight, Journal of Quantitative Spectroscopy and Radiative Transfer, 109, 52–73, https://doi.org/https://doi.org/10.1016/j.jqsrt.2007.07.007, 2008.

Bourassa, A. E., Rieger, L. A., Lloyd, N. D., and Degenstein, D. A.: Odin-OSIRIS stratospheric aerosol data product and SAGE III intercomparison, Atmospheric chemistry and physics, 12, 605–614, 2012.

Chen, Z., DeLand, M., and Bhartia, P. K.: A new algorithm for detecting cloud height using OMPS/LP measurements, Atmospheric Measurement Techniques, 9, 1239–1246, https://doi.org/10.5194/amt-9-1239-2016, 2016.

Deirmendjian, D.: Scattering and Polarization Properties of Water Clouds and Hazes in the Visible and Infrared, Appl. Opt., 3, 187–196, https://doi.org/10.1364/AO.3.000187, 1964.

Elash, B. J., Bourassa, A. E., Loewen, P. R., Lloyd, N. D., and Degenstein, D. A.: The Aerosol Limb Imager: acousto-optic imaging of limb-scattered sunlight for stratospheric aerosol profiling, Atmospheric Measurement Techniques, 9, 1261–1277, https://doi.org/10.5194/amt-9-1261-2016, 2016.

Grewal, M. S.: Kalman filtering : theory and practice, Prentice-Hall information and system sciences series, Prentice-Hall, Englewood Cliffs, N.J., ISBN 013211335X, 1993.

Hansen, J. E.: Multiple Scattering of Polarized Light in Planetary Atmospheres Part II. Sunlight Reflected by Terrestrial Water Clouds, Journal of Atmospheric Sciences, 28, 1400 – 1426, https://doi.org/10.1175/1520-0469(1971)028<1400:MSOPLI>2.0.CO;2, 1971.

Kalman, R. E.: A New Approach to Linear Filtering and Prediction Problems, Journal of Basic Engineering, 82, 35–45, https://doi.org/10.1115/1.3662552, 1960.

Kozun, M. N., Bourassa, A. E., Degenstein, D. A., and Loewen, P. R.: A multi-spectral polarimetric imager for atmospheric profiling of aerosol and thin cloud: Prototype design and sub-orbital performance, Review of Scientific Instruments, 91, 103 106, https://doi.org/10.1063/5.0016129, 2020.

Kozun, M. N., Bourassa, A. E., Degenstein, D. A., Haley, C. S., and Zheng, S. H.: Adaptation of the polarimetric multi-spectral Aerosol Limb Imager for high altitude aircraft and satellite observations, Appl. Opt., 60, 4325–4334, https://doi.org/10.1364/AO.419249, 2021.

Kulikova, M. V. and Tsyganova, J. V.: Improved discrete-time Kalman filtering within singular value decomposition, IET Control Theory & Applications, 11, 2412–2418, https://doi.org/https://doi.org/10.1049/iet-cta.2016.1282, 2017.

Letros, D., Bourassa, A., and Degenstein, D.: Kalman filtering approach to polarimetric calibration of an optical imager, Appl. Opt., 63, 4566–4582, https://doi.org/10.1364/AO.522809, 2024.

Malinina, E., Rozanov, A., Rozanov, V., Liebing, P., Bovensmann, H., and Burrows, J. P.: Aerosol particle size distribution in the stratosphere retrieved from SCIAMACHY limb measurements, Atmospheric measurement techniques, 11, 2085–2100, 2018.

McGee, L. A., Schmidt, S. F., and Center., A. R.: Discovery of the Kalman filter as a practical tool for aerospace and industry, National Aeronautics and Space Administration, Ames Research Center Moffett Field, Calif, http://purl.access.gpo.gov/GPO/LPS104644, 1985.

Rieger, L. A., Bourassa, A. E., and Degenstein, D. A.: Stratospheric aerosol particle size information in Odin-OSIRIS limb scatter spectra, Atmospheric measurement techniques, 7, 507–522, 2014.

https://doi.org/10.5194/egusphere-2025-67
Preprint. Discussion started: 31 March 2025

Rieger, L. A., Malinina, E. P., Rozanov, A. V., Burrows, J. P., Bourassa, A. E., and Degenstein, D. A.: A study of the approaches used to retrieve aerosol extinction, as applied to limb observations made by OSIRIS and SCIAMACHY, Atmospheric measurement techniques, 11, 3433–3445, 2018.

Rieger, L. A., Zawada, D. J., Bourassa, A. E., and Degenstein, D. A.: A Multiwavelength Retrieval Approach for Improved OSIRIS Aerosol Extinction Retrievals, Journal of geophysical research. Atmospheres, 124, 7286–7307, 2019.

Rodgers, C. D.: Inverse methods for atmospheric sounding : theory and practice, Series on atmospheric, oceanic and planetary physics ; v. 2, World Scientific Publishing Co. Pte. Ltd., ISBN 981022740X, 2000.

Taha, G., Loughman, R., Zhu, T., Thomason, L., Kar, J., Rieger, L., and Bourassa, A.: OMPS LP Version 2.0 Multi-wavelength Aerosol Extinction Coefficient Retrieval Algorithm, Atmospheric measurement techniques, 14, 1015–1036, 2021.

Thomason, L. W., Ernest, N., Millán, L., Rieger, L., Bourassa, A., Vernier, J.-P., Manney, G., Luo, B., Arfeuille, F., and Peter, T.: A global space-based stratospheric aerosol climatology: 1979–2016, Earth system science data, 10, 469–492, 2018.

Wang, L., Libert, G., and Manneback, P.: Kalman filter algorithm based on singular value decomposition, pp. 1224 – 1229 vol.1, https://doi.org/10.1109/CDC.1992.371522, 1992.

Zawada, D. J., Dueck, S. R., Rieger, L. A., Bourassa, A. E., Lloyd, N. D., and Degenstein, D. A.: High-resolution and Monte Carlo additions to the SASKTRAN radiative transfer model, Atmospheric Measurement Techniques, 8, 2609–2623, https://doi.org/10.5194/amt-8-2609-2015, 2015.

Zawada, D. J., Rieger, L. A., Bourassa, A. E., and Degenstein, D. A.: Tomographic retrievals of ozone with the OMPS Limb Profiler: algorithm description and preliminary results, Atmospheric measurement techniques, 11, 2375–2393, 2018.